Article   **Open Access**

Cath-KP, a novel peptide derived from frog skin, prevents oxidative stress damage in a Parkinson's disease model

Huanpeng Lu[1,3,4,#], Jinwei Chai[2,#], Zijian Xu[1,3,4], Jiena Wu[2], Songzhe He[1,3,4], Hang Liao[2], Peng Huang[1,3,4], Xiaowen Huang[5], Xi Chen[1,3,4], Haishan Jiang[1], Shaogang Qu[6,1,3,4,*], Xueqing Xu[2,*]

[1] *Department of Neurology, Nanfang Hospital, Southern Medical University, Guangzhou, Guangdong 510515, China*

[2] *Guangdong Provincial Key Laboratory of New Drug Screening, School of Pharmaceutical Sciences, Southern Medical University, Guangzhou, Guangdong 510515, China*

[3] *Guangdong-Hong Kong-Macao Greater Bay Area Center for Brain Science and Brain-Inspired Intelligence, Guangzhou, Guangdong 510515, China*

[4] *Key Laboratory of Mental Health of the Ministry of Education, Southern Medical University, Guangzhou, Guangdong 510515, China*

[5] *Department of Dermatology, Nanfang Hospital, Southern Medical University, Guangzhou, Guangdong 510515, China*

[6] *Department of Neurology, Ganzhou Hospital-Nanfang Hospital, Southern Medical University, Ganzhou, Jiangxi 341001, China*

ABSTRACT

Parkinson's disease (PD) is a neurodegenerative condition that results in dyskinesia, with oxidative stress playing a pivotal role in its progression. Antioxidant peptides may thus present therapeutic potential for PD. In this study, a novel cathelicidin peptide (Cath-KP; GCSGRFCNLF NNRRPGRLTLIHRPGGDKRTSTGLIYV) was identified from the skin of the Asiatic painted frog (*Kaloula pulchra*). Structural analysis using circular dichroism and homology modeling revealed a unique $\alpha\beta\beta$ conformation for Cath-KP. *In vitro* experiments, including free radical scavenging and ferric-reducing antioxidant analyses, confirmed its antioxidant properties. Using the 1-methyl-4-phenylpyridinium ion (MPP^+)-induced dopamine cell line and 1-methyl-4-phenyl-1,2,3,6-tetrahydropyridine (MPTP)-induced PD mice, Cath-KP was found to penetrate cells and reach deep brain tissues, resulting in improved MPP^+-induced cell viability and reduced oxidative stress-induced damage by promoting antioxidant enzyme expression and alleviating mitochondrial and intracellular reactive oxygen species accumulation through Sirtuin-1 (Sirt1)/Nuclear factor erythroid 2-related factor 2 (Nrf2) pathway activation. Both focal adhesion kinase (FAK) and p38 were also identified as regulatory elements. In the MPTP-induced PD mice, Cath-KP administration increased the number of tyrosine hydroxylase (TH)-positive neurons, restored TH content, and ameliorated dyskinesia. To the best of our knowledge, this study is the first to report on a cathelicidin peptide demonstrating potent antioxidant and neuroprotective properties in a PD model by targeting oxidative stress. These findings expand the known functions of cathelicidins, and hold promise for the development of therapeutic agents for PD.

Keywords: Cath-KP; Peptide; Parkinson's disease; Oxidative stress; Neuroprotection

INTRODUCTION

Parkinson's disease (PD), related to excessive levels of reactive oxygen species (ROS) and oxidative injury, is the most prevalent neurological condition worldwide after Alzheimer's disease (Bloem et al., 2021). In 2005, the number of PD patients over 50 years of age in the 10 most populous countries was 4.6 million, which is expected to increase to 9.3 million by 2030 (Dorsey et al., 2007). Current medications are unable to halt degenerative progression in PD patients, emphasizing the necessity for the identification and development of novel, efficacious, and safe therapeutic compounds. Neuropathologically, PD is characterized by the formation of intracytoplasmic Lewy bodies and the selective and progressive loss of dopaminergic (DA) neurons in the substantia nigra pars compacta (SNpc) (Bloem et al., 2021). While the precise etiology of PD remains unclear, imbalanced redox homeostasis derived from mitochondrial dysfunction and/or dopamine metabolism underpins both sporadic and

idiopathic manifestations (Bloem et al., 2021). Furthermore, various environmental toxins, such as 1-methyl-4-phenyl-1,2,3,6-tetrahydropyridine (MPTP), 6-hydroxydopamine, and rotenone, can compromise mitochondrial functionality, induce DA neuron damage, and produce PD-like motor neurological symptoms (Dauer & Przedborski, 2003). For example, following systemic exposure, highly lipophilic MPTP can rapidly cross the blood-brain barrier (BBB), convert into 1-methyl-4-phenylpyridinium ions (MPP^+) in astrocytes, and suppress mitochondrial respiratory complex I (first enzyme of the respiratory chain) within the mitochondria (Zeng et al., 2020b). This can lead to diminished adenosine triphosphate (ATP) generation and mitochondrial membrane potential ($\Delta\psi m$), as well as increased ROS formation, especially superoxide (O_2^-), which can induce mitochondrial malfunction and fragmentation, oxidative stress, and even death (Bloem et al., 2021; Dauer & Przedborski, 2003). Many cell death-related pathways, such as apoptosis, cell necrosis, and ferroptosis, are associated with oxidative stress (Callizot et al., 2019; Li et al., 2023; Qu et al., 2022). Among them, apoptosis is considered the predominant programmed cell death mechanism associated with PD (Tatton et al., 2003). Similarly, dopamine metabolism is implicated in the increased production of ROS in PD patients, thereby enhancing the susceptibility of DA neurons to oxidative injury (Vidoni et al., 2018). Therefore, antioxidants that are effective at scavenging excessive free radicals or limiting their production have received increasing attention in PD treatment due to the significant role of ROS in this disease.

Amphibians inhabit harsh environments characterized by a multitude of potential threats, including pathogenic microbes, parasites, and physical and chemical stressors. Therefore, their skin has evolved numerous glands that secrete diverse defensive molecules, including peptides, a noted resource for novel drug development (Mwangi et al., 2019; Qi et al., 2019; Xu & Lai, 2015) or as important channels (Zhang et al., 2021). Cathelicidins, unique to vertebrates, are multifaceted defense peptides essential for immune regulation, inflammatory response, wound healing, and blood vessel formation. Since the discovery of cathelicidin-AL in *Amolops loloensis* in 2012 (Hao et al., 2012), more than 20 cathelicidins from 13 amphibian species have been reported. These peptides exhibit a range of biological functions, including antimicrobial, antioxidant, lipopolysaccharide (LPS) neutralization, chemotaxis, antitumor, and wound healing activities (Cao et al., 2018; Chai et al., 2021; Wei et al., 2013). While certain cathelicidins, e.g., cathelicidin-PN (*Pelophylax nigromaculata*) (Wang et al., 2021), cathelicidin-NV (*Nanorana ventripunctata*) (Feng et al., 2022), cathelicidin-OA1 (*Odorrana andersonii*) (Cao et al., 2018), and cathelicidin-HR (*Hoplobatrachus rugulosus*) (Wiriyaampaiwong et al., 2022), are known to exhibit *in vitro* free radical scavenging and antioxidant activity (Xu & Lai, 2015), their therapeutic effects and mechanisms regarding neurodegenerative diseases, especially PD, remain unexplored.

The Asiatic painted frog (*Kaloula pulchra*: Microhylidae), characterized by a triangular-shaped body (55–77 mm long in males and 56–76 mm long in females), is predominantly found in low-altitude areas of South China and Southeast Asia (Fei et al., 2012). Upon disturbance or capture, these frogs inflate their bodies to a near-spherical shape and secrete a protective white substance from their skin (Zhang et al., 2010). Microhylid species, including *K. pulchra*, have been used in traditional Chinese medicine for several centuries to alleviate symptoms described as "dispelling wind", a condition associated with PD (Fauna CGOCMA, 1983). While previous research has identified an antimicrobial peptide (brevinin-2KP) and two trypsin inhibitors from the skin of microhylids (Conlon & Kim, 2000; Gao et al., 2022; Zhang et al., 2010), no studies have explored the presence of cathelicidins or antioxidants. In this research, a novel cathelicidin (Cath-KP) with potent antioxidant effects was identified from *K. pulchra* frog skin secretions. Based on circular dichroism (CD) and homology modeling, the secondary structure of the identified peptide was determined. *In vitro* antioxidant properties were assessed using 2,2'-azinobis-(3-ethylbenzthiazoline-6-sulphonate) (ABTS) and 1,1-diphenyl-2-picrylhydrazyl (DPPH) radical scavenging assays and ferric-reducing antioxidant power (FRAP) analysis. The possible role of Cath-KP in neurological diseases was explored by examining its underlying mechanisms and effects on viability, delivery, mitochondrial $\Delta\psi m$, and ROS accumulation in MPP^+-induced MN9D cells. The neuroprotective effects of Cath-KP in MPTP-induced PD mice were also evaluated. To the best of our knowledge, this is the first cathelicidin demonstrated to show potent antioxidant and neuroprotective properties in PD mice by targeting oxidative stress. These findings may help guide the development of innovative PD therapeutic agents and expand our understanding of the biological functions of cathelicidins.

MATERIALS AND METHODS

Reagents and cells
Anti-TH (F-11, sc-25269), SOD-1 (24, sc-101523), SOD-2 (E-10, sc-137254), and HO-1 (F-4, sc-390991) antibodies were obtained from Santa Cruz Biotechnology (USA). Nrf2 (ab137550), Keap1 (ab227828), Bcl-2 (ab182858), and anti-histone H3 (ab1791) antibodies were obtained from Abcam (UK). Sirt1 (#9475), phospho-FAK (#3283), FAK (#13009), phospho-p38 (#4511), and p38 (#14451) antibodies were purchased from Cell Signaling Technology (USA). Bax (50599-2-Ig) was purchased from Proteintech Group (USA). Human integrin α1 (FAB56761G) and β1 (FAB17781G) 488-conjugated antibodies were purchased from R&D Systems (USA). The GAPDH antibody (AB0037) was purchased from Abways Technology (China). Goat anti-mouse IgG (H+L) (DyLight 488 conjugate) (BA1126), goat anti-mouse IgG (H+L) (DyLight 550 conjugate) (BA1133), and goat anti-rabbit IgG (H+L) (DyLight 550 conjugate) (BA1135) secondary antibodies were purchased from Boster Biological Technology (USA). Tubulin antibody (AT819), actin antibody (AA128), horseradish peroxidase (HRP)-labeled goat anti-rabbit IgG (H+L) secondary antibody, and HRP-labeled goat anti-mouse IgG (H+L) secondary antibody were purchased from Beyotime Biotechnology (China). MPTP (M0896) and MPP^+ (D048) were obtained from Sigma-Aldrich (USA). Cath-KP and fluorescein isothiocyanate (FITC)-Cath-KP (>95% purity) were synthesized, purified, and confirmed by GL Biochemistry (China). The mouse DA neuronal cell line (MN9D) was obtained from the American Type Culture Collection (ATCC, USA) and maintained in Dulbecco's Modified Eagle Medium (DMEM, Gibco, USA) with 10% fetal bovine serum (FBS, Gibco, USA) and 1% penicillin-streptomycin-amphotericin B solution (P7630, Solarbio, China) in an incubator at 37 °C and 5% CO_2. Human umbilical vein endothelial cells (HUVECs) obtained from ATCC were maintained in DMEM-F12 (Gibco,

USA) with 10% FBS, growth factors, and 1% penicillin-streptomycin-amphotericin B solution in an incubator at 37 °C and 5% CO_2. The Sirtuin-1 (Sirt1)-specific inhibitor EX527 (Sl541, Selleck, USA) was dissolved in dimethyl sulfoxide (DMSO).

Animals and ethical statement

Adult *K. pulchra* specimens (weighing 40–60 g) were collected from Baiyun District, Guangzhou City, Guangdong Province, China, and humanely sacrificed. Their skin tissue was immediately removed and placed in liquid nitrogen until use. Male C57BL/6 mice (8–10 weeks old, 25–30 g) were obtained from BesTest Bio-Tech Co., Ltd. (Zhuhai, China) and housed at the experimental animal center at Southern Medical University under a 12:12 h light/dark cycle at 25±2 °C and 55%±10% humidity, with free access to food and water. Prior to the studies, the animals were given at least one week to acclimatize to their new environment. All animal procedures were authorized by the Animal Care and Use Ethics Committee of Nanfang Hospital (NFYY-2021-1074).

Molecular cloning and sequence analyses

Molecular cloning of Cath-KP-encoding cDNA followed our previous studies, with minor modification (Chai et al., 2021; Zeng et al., 2018). In brief, after obtaining the 5' fragments of cDNA encoding the Cath-KP precursor through polymerase chain reaction (PCR) amplification using the primer encoding the cathelin domain and the 5' PCR primer from the SMART cDNA Library Construction Kit, a sense primer (5'-AAATG CAGAGCTGCTGGTGGGGGGC-3') was synthesized and coupled to the 3' PCR primer CDS III from the same kit to screen the full cDNA encoding Cath-KP. SignalP v.6.0 (http://www.cbs.dtu.dk/services/SignalP) was used to predict the signal peptide. The Bioinformatics Resources Portal (http://www.expasy.org/tools/) was used to determine the physicochemical characteristics of Cath-KP. The Basic Local Alignment Search Tool (BLAST) was used to identify cathelicidin sequences with high homology to Cath-KP, which were then aligned using ClustalW (http://embnet.vital-it.ch/software/ClustalW.html). PEP-FOLD v.3.5 (http://bioserv.rpbs.univ-paris-diderot.fr/services/PEP-FOLD3) was used to predict the structure of Cath-KP.

CD analysis

The secondary structure and stability of Cath-KP under different solvent conditions were determined using a Chirascan-plus CD spectrophotometer (Applied Photophysics, UK). Spectra (180–260 nm) were determined in a cuvette with a 0.1 cm path length, bandwidth of 1 nm, response time of 1 s, scan rate of 100 nm/min, and temperature of 25 °C. Cath-KP was dissolved in 0, 30, 60, and 90 mmol/L sodium dodecyl sulfate (SDS) solution or 60 mmol/L SDS solution with 0, 100, 200, and 400 mmol/L NaCl at a final concentration of 50 µmol/L. To further determine the effect of temperature on secondary structure stability, Cath-KP (final concentration of 50 µmol/L) was dissolved in 60 mmol/L SDS and incubated at 25, 37, 50, 70, and 90 °C for 1 h before measuring the CD spectra. The CD data (deg·cm^2/dmol) were reported as the mean residual ellipticity (θ) of two successive scans.

Measurement of antioxidant activities *in vitro*

ABTS (S0119, Beyotime Biotechnology, China) and DPPH (Sigma-Aldrich, USA) radical scavenging activity assays were performed as reported previously, with slight modifications (Zeng et al., 2020a). In brief, 10 µL of phosphate-buffered saline (PBS) or Cath-KP (final concentrations ranging from 2.5–40 µmol/L) was added to a 96-well plate containing 200 µL of ABTS$^+$ or DPPH working solution and left at room temperature for 16 min and 9 min, respectively. Absorbance was detected at 734 nm and 517 nm using a microplate reader (Infinite M1000 Pro, Tecan, Switzerland). Total reducing power of Cath-KP was evaluated using a FRAP Kit (S0116, Beyotime Biotechnology, China) according to the methods described in our prior research, with minor modification (Zeng et al., 2020a). Briefly, 5 µL of PBS or Cath-KP (final concentrations ranging from 2.5–40 µmol/L) was added to a 96-well plate with 180 µL of FRAP working solution and left at room temperature for 5 min. Absorbance was detected at 593 nm using a microplate reader. Total antioxidant capacity was determined using a standard curve and expressed as the equivalent concentration of $FeSO_4$ solution. All assays were performed in triplicate.

PD mouse model induction

A MPTP-induced PD mouse model was established to examine the potential neuroprotective effects of Cath-KP based on previous reports (Zhang et al., 2017). In brief, mice were administered an intraperitoneal injection of MPTP at a dose of 30 mg/kg at around 0800h for 5 consecutive days to establish a subacute PD mouse model. Control mice were administered an intraperitoneal injection of sterilized 0.9% saline. Simultaneously, mice were continuously administered an intraperitoneal injection of 1 mg/kg of Cath-KP and 0.9% saline at approximately 1600h for 6 consecutive days. On day 9 after the first dose, behavioral tests, including open field, grasping, pole, and rotarod tests, were carried out to assess mobility and anxiety, upper limb locomotion, anti-fatigue ability, and motor coordination of mice. On day 12 after the first dose, mice were anesthetized with 1% sodium pentobarbital (50 mg/kg; Ceva Santé Animale, France). Blood was removed with sterilized 0.9% saline and their brain tissues were quickly removed for immunohistochemical, immunofluorescence, and western blot analyses.

Behavioral study

All tests were performed between 0900h and 1400h and were assessed by the same rater in an observation room under low-intensity light. The mice were acclimated for at least 1 h prior to the start of the tests. To prevent olfactory cues, all equipment was cleaned with 10% ethanol between each animal test.

Open field test: An open field test was conducted to assess both movement and anxiety-related behaviors in mice. Each mouse was individually placed at the center of a box (50 cm×50 cm×40 cm) and videotaped for 10 min using EthoVision XT software (China). Parameters such as total distance traveled, total duration of activity, and distance traveled in the center were noted.

Grasping test: A grasping test was used to assess the motor capacity of the forelimbs of mice. In brief, mice were suspended by their two front paws on a horizontal cable (diameter 1 mm, 30 cm from the ground). The duration for which the mice remained suspended was recorded.

Rotarod test: An accelerated rotarod test was used to determine endurance capacity of mice. In brief, mice were trained twice daily for three days on a TSE Rotarod (TSE Systems, Bad Homburg, Germany) at a speed of 5 r/min. In the formal experiments, the time to fall was recorded as the speed of the spinning rod gradually accelerated from 0 to 30

r/min over 5 min.

Pole-climbing test: A pole-climbing test was implemented to assess motor coordination of the mice. In brief, mice were positioned at the top of a vertical pole (55-cm length, 1-cm diameter), facing downwards. Prior to the formal experiment, mice received three days of training. The total time required to descend to the base was recorded.

Cell viability assay

MN9D cells ($3×10^3$ cells/well) were grown in 96-well plates (Corning, Germany) for 24 h at 37 °C, then incubated with Cath-KP (0–5 µmol/L), MPP^+ (0– 1 mmol/L), and MPP^+ (1 mmol/L) plus Cath-KP (0–5 µmol/L) for another 24 h at 37 °C. After that, cell viability was determined using CCK-8 reagent (C0037, Beyotime Biotechnology, China) following the manufacturer's manual. A multifunctional microwell plate tester (Infinite 200 Pro, Tecan Group AG, Switzerland) was used to detect absorbance at 450 nm. All experiments were repeated at least three times.

Intracellular ROS detection of live cells

The conversion of non-fluorescent 2,7-dichlorodihydrofluorescein (DCFH) to fluorescein by intracellular ROS can serve as the basis for measuring intracellular ROS, with increased levels reflected by fluorescence intensity. Here, MN9D cells seeded in black 96-well plates ($3×10^3$ cells/well) were washed with PBS three times and stained with 20 µmol/L DCFH-DA (S0033M, Beyotime Biotechnology, China) for 2 h at 37 °C after the incubation experiments (Chai et al., 2022). Intracellular fluorescence intensities were measured using an IX73 Inverted Microscope (Olympus, Japan) and FACScan flow cytometry (Becton Dickinson Company, USA).

Mitochondrial ROS detection of live cells

MN9D cells ($3×10^3$ cells/well) were treated with 1 mmol/L MPP^+ and/or 5 µmol/L Cath-KP for an additional 24 h after being grown in 96-well plates for 24 h at 37 °C. MitoSOX (M36008, Thermo Fisher Scientific, USA) and Hoechst 33258 staining (C1017, Beyotime Biotechnology, China) solutions were added. After incubation for 15 min at 37 °C, the cells were washed three times, and images were scanned using an IX73 Inverted Microscope (Olympus, Japan).

Mitochondrial *Δψm* detection of live cells

MN9D cells ($3×10^3$ cells/well) were treated with 1 mmol/L MPP^+ and/or 5 µmol/L Cath-KP for an additional 24 h after being grown in 96-well plates for 24 h at 37 °C. The cells were then stained with JC-1 (C2003S, Beyotime Biotechnology, China) after washing three times with PBS (pH 7.4). The *Δψm* of labeled cells was determined using flow cytometry or fluorescence microscopy, with green fluorescence signals (J-Monomers) indicating low *Δψm* and red fluorescence signals (J-Aggregates) indicating high *Δψm*.

Intracellular superoxide dismutase (SOD), catalase (CAT), and nitric oxide (NO) detection assays

MN9D cells ($3×10^5$ cells/well) were treated with 1 mmol/L MPP^+ and/or 5 µmol/L Cath-KP for an additional 24 h after being grown in 6-well plates for 24 h at 37 °C. The cells were then collected and split with RIPA lysis buffer (P0013, Beyotime Biotechnology, China). According to the manufacturer's instructions, levels of SOD, CAT, and NO were detected using assay kits (Cu/Zn-SOD and Mn-SOD Assay Kit with WST-8 (S0103), Catalase Assay Kit (S0051), and Nitrate/Nitrite Assay Kit (S0023), respectively) from Beyotime Biotechnology (China).

Immunohistochemistry and immunofluorescence assays

A freezing microtome (CM1950, Leica, Germany) was used to slice embedded mouse brains into 7 µm slices, which were then incubated with appropriate primary antibodies overnight at 4 °C. After that, brain slices were treated with fluorescent-labeled secondary antibodies and 4',6-diamidino-2-phenylindole (DAPI) for the immunofluorescence test. Images were scanned using a confocal laser scanning microscope (LSM 980, Zeiss, Germany). Quantitative analyses were carried out using ImageJ software. For immunohistochemical analysis, the brain slices were exposed to biotin-tagged secondary antibodies and stained with diaminobenzidine (DAB). Stereomicroscopy (N23977, Zeiss, Germany) was used to scan the images.

Western blot assay

MN9D cells ($3×10^5$ cells/well) were treated with 1 mmol/L MPP^+ and/or 5 µmol/L Cath-KP for an additional 24 h after being seeded into 6-well plates for 24 h. Total proteins were extracted from the cells and substantia nigra tissue using RIPA lysis buffer (P0013, Beyotime Biotechnology, China), then quantified using a BCA Protein Assay Kit (P0010, Beyotime Biotechnology, China) before western blotting was carried out according to our previous study (Chai et al., 2021). Primary antibodies against TH, B-cell lymphoma 2 (Bcl-2), Bcl-2 associated X (Bax), Sirt1, Nuclear factor erythroid 2-related factor 2 (Nrf2), Heme oxygenase 1 (HO-1), Kelch-like ECH-associated protein 1 (Keap1), SOD-1, SOD-2, phospho-focal adhesion kinase (FAK), FAK, phospho-p38, p38, actin, Glyceraldehyde 3-phosphate dehydrogenase (GAPDH), histone H3, tubulin, and HRP-conjugated secondary antibodies were applied for western blot analysis. Immobilon western chemiluminescent HRP substrate (Millipore, USA) was used to incubate the attached antibodies, and Tanon 5200 (China) was used to detect chemiluminescence. ImageJ was used to determine optical density of the bands. All experiments were performed in triplicate.

Peptide internalization analysis

For fluorescence intensity detection, MN9D cells ($1×10^5$ cells/well) were cultured overnight in 24-well plates, then subsequently treated with FITC-Cath-KP (0, 2.5, and 5 µmol/L) for 3 h at 4 °C or 37 °C and assayed using confocal laser scanning microscopy (LSM 980, Zeiss, Germany) and FACScan flow cytometry (Becton Dickinson Company, USA). To evaluate its effect of heparin sulphate on FITC-Cath-KP internalization, heparin sulphate (50 µg/mL) was preincubated with 5 µmol/L FITC-Cath-KP for 30 min, followed by co-incubation with the cells for another 3 h and flow cytometry analysis. All experiments were performed in triplicate.

Assessment of brain targeting delivery

Male C57BL/6 mice received an intraperitoneal injection of FITC-Cath-KP (1 mg/kg) and were then anesthetized at 0, 2, and 6 h post-injection with 1% sodium pentobarbital. Blood was removed with sterilized 0.9% saline and 4% paraformaldehyde via cardiac perfusion. Brains were surgically removed, embedded in paraffin, cut into 7 µm sections using a Leica CM1950 freezing microtome, and stained with tyrosine hydroxylase (TH) antibodies and DAPI. The SNpc slices were immediately scanned using an IX73 Inverted Microscope (Olympus, Japan). Control mice received an intraperitoneal injection of sterilized 0.9% saline.

Statistical analysis

Statistical analyses were performed using GraphPad Prism v.9.0 (GraphPad Software, USA). All data were evaluated using unpaired Student's *t*-test and ordinary one-way analysis of variance (ANOVA) with Bonferroni's multiple comparison test. Ten individuals from each group were used for the behavioral tests. Three to five samples from each group were used for *in vivo* immunofluorescence, immunohistochemical, and western blot analyses. Three individuals per group were employed for *in vitro* western blot and immunofluorescence assays. Values are given as mean±standard error of the mean (SEM). Significant *P*-values were determined at [*]: *P*<0.05; [**]: *P*<0.01; [***]: *P*<0.001; [****]: *P*<0.0001.

RESULTS

Identification and structural analysis of Cath-KP

The cDNA sequence of Cath-KP was derived from *K. pulchra* skin using a PCR-based technique. As shown in Figure 1A, the Cath-KP precursor, encoded by 540 base pairs, consisted of 169 amino acid residues and shared high sequence similarity to antimicrobial peptides (AMPs) in the cathelicidin family based on a NCBI BLAST search and sequence alignment, showing 58.49%, 57.89%, and 57.89% homologies with cathelicidin-HR (*H. rugulosus*), cathelicidin-PY1 (*Paa yunnanensis*), and cathelicidin-NV (*N. ventripunctata*), respectively (Figure 1B). However, the mature peptide, named Cath-KP (GCSGRFCNLFNNRRPGRLTLIHRPGGDKRTS TGLIYV) after its classical RR protease cleavage site, showed no similarity with any reported AMP (Figure 1B). The theoretical isoelectric point (PI) of Cath-KP was 11.35, indicating a positive charge under physiological conditions.

The relative mass of Cath-KP was 4 131.70 Da, while the relative mass of FITC-Cath-KP was 4 636.35 Da (Supplementary Figure S1).

The structure of Cath-KP was predicted using the PEP-FOLD3 method. The structure exhibited an *αββ* conformation, with an *α*-helix (Arg-5-Asn-11) in the N-terminal and a *β*-hairpin (Leu-18-Asn-Val-37) at the C-terminal (Figure 1C). Notably, an RTS sequence, typically recognized as a disintegrin motif, was located in the loop between two *β*-strands. Consistent with the predicted results, Cath-KP in aqueous solution showed a broad negative peak near 200 nm, indicative of an unfolded peptide in equilibrium with a *β*-sheet structure (Eiríksdóttir et al., 2010). Upon dissolution in SDS solution, the negative minimum of Cath-KP shifted from 200 nm to 206 nm, indicative of enhanced secondary structure formation. Results from CD spectral analysis showed that Cath-KP contained 5.40% *α*-helices, 38.30% *β*-sheets, 21.90% turns, and 38.30% random coils in aqueous solution, with the *α*-helix ratio increasing gradually with SDS concentration from 5.40% to 7.80% (Figure 1D; Supplementary Table S1). As shown in Figure 1E, F and Supplementary Table S1, increasing NaCl concentrations disrupted the secondary structure components of Cath-KP, as evidenced by the increase in *α*-helix ratio and decrease in *β*-sheet ratio. In contrast, increasing temperature resulted in minimal alterations in CD spectra, indicating that Cath-KP was stable at high temperature but sensitive to high salt concentrations.

Cath-KP improved motor performance in MPTP-treated mice and reversed DA neuron loss

The prominent clinical manifestation of PD is the impairment of motor function. Prior to the formal experiments, preliminary
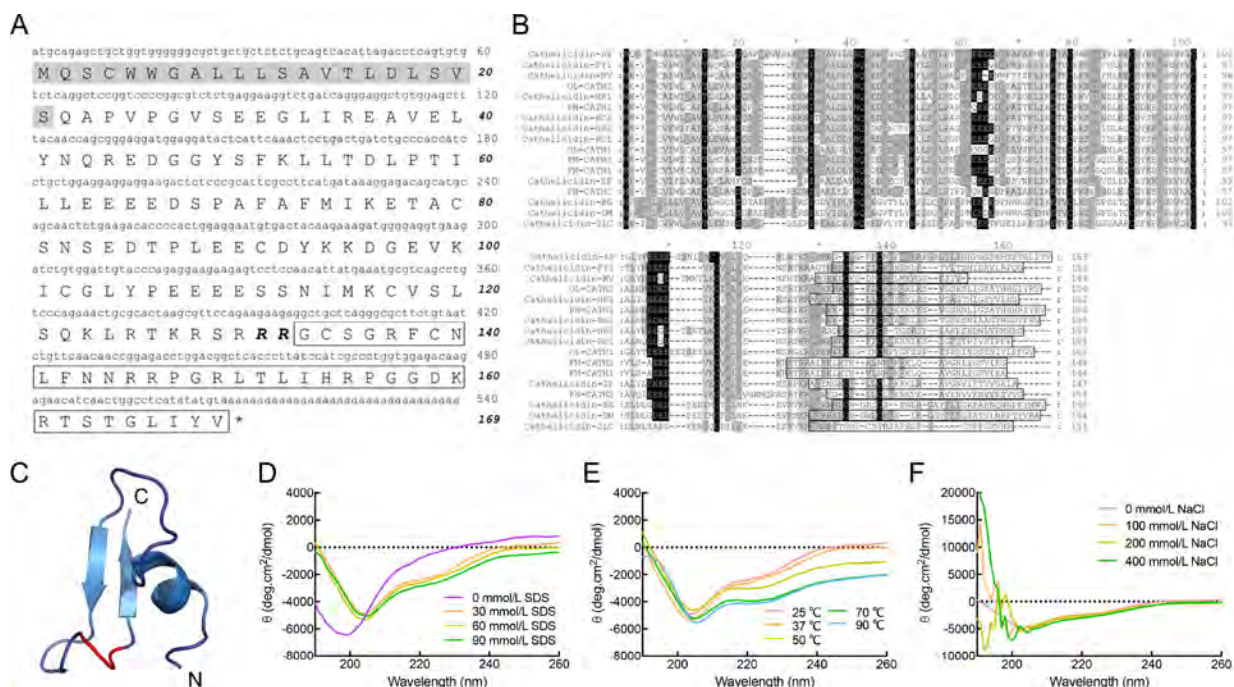

Figure 1 Sequence characterization and secondary structure determination of Cath-KP

A: cDNA encoding Cath-KP and deduced amino acid sequences. Signal peptide is marked in gray, RR residues are shown in bold and italic. Mature peptide sequence is boxed, and stop codon is denoted by an asterisk (*). Nucleotide and amino acid numbers are shown after sequence. B: Alignment of cathelicidin peptides from amphibians. To better present sequence identity, hyphens (-) have been added to some sequences to indicate residue deletion. Same and highly conserved residues are represented in black and shadows, respectively. All mature peptide domains are boxed. C: Cartoon image of Cath-KP conformation with labeled N and C termini and RTS motif in red. CD spectra of Cath-KP dissolved in: D: SDS solutions; E: temperatures; or F: NaCl solutions.

animal studies were conducted using varying doses of Cath-KP (0.5, 1, and 2 mg/kg) to determine the most appropriate dosage for use *in vivo*. As shown in Supplementary Figure S2, 1 mg/kg of Cath-KP yielded the best improvement in dyskinesia in PD mice. Furthermore, no significant hepatic or renal toxicity was observed in the mice at this dose (Supplementary Figure S3). Thus, 1 mg/kg of Cath-KP was selected as the optimal concentration for subsequent animal experiments. The open field, grasping, pole, and rotarod tests were used to assess the effects of Cath-KP on MPTP-induced motor impairment in mice (Figure 2A). As shown in Figure 2B, MPTP administration markedly decreased locomotor activity in the open field test. Furthermore, total distance of spontaneous motion, number of spontaneous activities, and central distance of spontaneous motion in MPTP-treated mice decreased by 50.00%, 23.52%, and 69.95%, respectively, compared to the control group in the open field test(Figure 2C–E), suggesting

that MPTP exposure impaired motor coordination. Additionally, compared to the corresponding control groups, MPTP injection led to reductions in the average holding time and time spent on the rotarod by 76.78% and 69.03%, respectively (Figure 2F, G). The pole-climbing test was utilized to evaluate mouse coordination and balance. Results revealed that the MPTP administration extended the pole-climbing time by 153.25% relative to the control group (Figure 2H). In comparison to the MPTP-only group, Cath-KP treatment at 1 mg/kg ameliorated motor dysfunction in PD mice. Notably, total distance of spontaneous motion increased from 16.17 m to 26.24 m, number of spontaneous activities increased from 865.80 to 1 009.10, and central distance of spontaneous motion increased from 1.78 m to 4.32 m in the open field test (Figure 2C–E), average holding time and time spent increased from 6.20 s to 16.10 s and 32.80 s to 75.80 s in the grasping and rotarod tests (Figure 2F, G), while climbing time
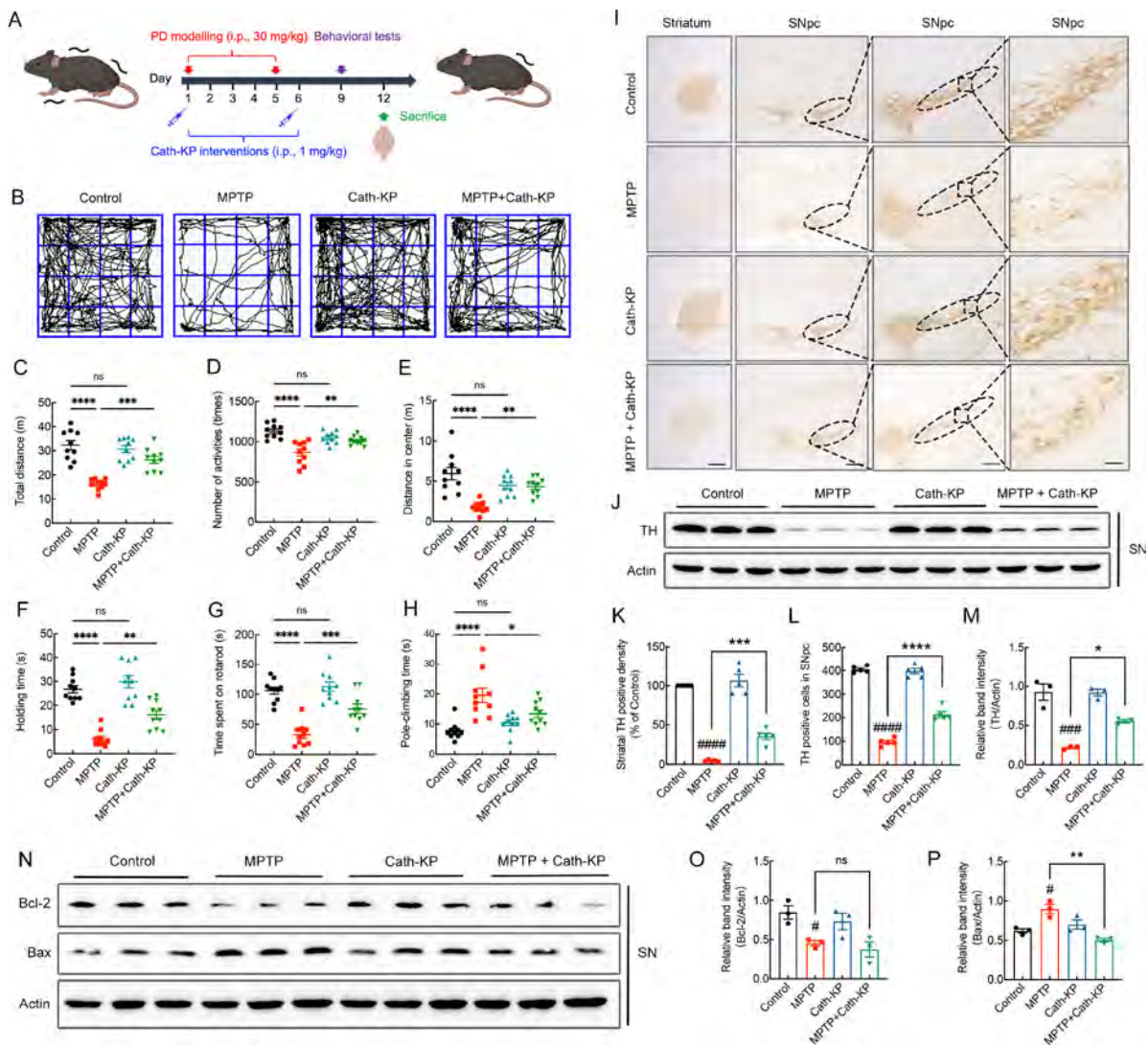

Figure 2 Cath-KP decreased motor dysfunction and dopaminergic (DA) neuron degeneration in Parkinson's disease (PD) mice

A: Experimental design involving Cath-KP treatment (intraperitoneal (i.p.) 1 mg/kg/day) in MPTP-induced PD mice (i.p. 30 mg/kg/day). B: Travelled trace in open area. C–E: Analysis of total distance, number of activities, and central distance in open field test (*n*=10). F–H: Analysis of grasping, rotarod, and pole-climbing tests (*n*=10). I, K, L: Immunohistochemical staining and analysis of TH-positive neurons in the striatum and SNpc (*n*=5). Borders of the SNpc are shown by ellipses and the box represents further enlarged area. Scale bar: 1 mm for images in the striatum; 800, 100, and 50 μm for images in the SNpc (from left to right). J, M–P: Representative western blot images and analysis of TH, Bax, and Bcl-2 expression levels in the SNpc (*n*=3). Data are represented as means±SEM with ordinary one-way ANOVA. ns: Not significant. #: $P<0.05$, ###: $P<0.001$, and ####: $P<0.0001$ vs. Control. *: $P<0.0001$ vs. Control. *: $P<0.05$, **: $P<0.01$, ***: $P<0.001$, and ****: $P<0.0001$ vs. PD models.

decreased from 19.50 s to 13.40 s in the pole-climbing test (Figure 2H). Thus, these findings demonstrate the potential benefits of Cath-KP in treating motor dysfunction.

The primary pathological feature of PD is the loss of DA neurons in the SNpc and a consequent reduction in dopamine levels in the striatum. The potential protective effects of Cath-KP on DA neurons in the SNpc following MPTP administration were assessed. As shown by TH immunohistochemical analysis (Figure 2I), SNpc DA neuronal degeneration was clearly observed in the brains of the MPTP group. Post-MPTP exposure, a marked decrease in DA neurons was detected, as evidenced by immunohistochemical analysis of TH-positive cell terminals in the striatum (Figure 2K) and SNpc (Figure 2L). These findings were confirmed by western blot analysis (Figure 2J), revealing a 76.62% reduction in TH protein expression in the model group compared to the control group (Figure 2M). Notably, Cath-KP treatment reversed these changes both histologically (725.87% increase in the striatum and 120.95% increase in the SNpc) and at the protein expression level (2.57-fold increase in the SNpc).

To explore whether the protective effects of Cath-KP on DA neuron loss induced by MPTP in the SNpc were associated with its anti-apoptotic effects, the concentrations of Bax and Bcl-2 in the SNpc were determined by western blot analysis. As illustrated in Figure 2N–P, MPTP exposure significantly reduced Bcl-2 expression but increased Bax expression, and thus induced apoptosis in the SNpc. Cath-KP treatment reversed the MPTP-induced changes in Bax protein expression in the SNpc, but not that of Bcl-2 (Figure 2N–P). These findings suggest that the protective effects of Cath-KP against PD are, at least partially, mediated by inhibition of SNpc apoptosis.

Cath-KP enhanced TH expression in MPP$^+$-induced MN9D cells

To further explore the protective mechanism of Cath-KP against MPTP-induced DA neuron loss in mice, we assessed its effects on TH expression, a cytoplasmic marker of DA neurons (Daubner et al., 2011), in MN9D cells. As depicted in Figure 3A, B, the cultured MN9D cells exhibited TH-positive staining and showed a 76.99% reduction in fluorescence intensity after MPP$^+$ treatment relative to the control group. Notably, this reduction in MPP$^+$-treated cells was ameliorated (2.04-fold increase) following Cath-KP treatment, which did not affect the MN9D cells without MPP$^+$ treatment when comparing the model and control groups. Furthermore, western blot analysis demonstrated a 45.89% decrease in TH protein content in the MN9D cells exposed to MPP$^+$ compared to the control group; however, Cath-KP treatment significantly attenuated this reduction by 1.59-fold (Figure 3C, D). These results not only validate the utility of MN9D cells for subsequent mechanistic studies but also suggest that Cath-KP offers neuronal protection against MPP+ damage.

Decreased TH levels are closely associated with the progression of DA neuron death (Daubner et al., 2011). To further explore whether Cath-KP can mitigate the death of MN9D cells induced by MPP$^+$, cell viability was measured. As shown in Figure 3E, Cath-KP did not exhibit cytotoxicity to MN9D cells, even at doses of 5 µmol/L after 24 h. Furthermore, MPP$^+$ inhibited MN9D cell proliferation concentration dependently, with an EC_{50} value of approximately 1 mmol/L (Figure 3F). In contrast, Cath-KP attenuated the cytotoxic effects of MPP$^+$ on MN9D cells in a concentration-dependent manner, with cell viabilities

enhanced by 2.37%, 32.33%, and 60.85% when co-incubated with 1.25, 2.5, and 5 µmol/L of Cath-KP and 1 mmol/L of MPP$^+$ for 24 h (Figure 3G). To explore the mechanism by which Cath-KP suppressed MPP$^+$-induced DA neuron death, MN9D cell apoptosis was analyzed. As illustrated in Figure 3H–J, treatment with MPP$^+$ markedly reduced Bcl-2 expression and increased Bax expression, thus inducing MN9D cell apoptosis. However, Cath-KP administration reversed the MPP$^+$-induced changes in Bcl-2 and Bax protein expression in the MN9D cells (Figure 3H–J). Together, these findings indicate that the neuroprotective effects of Cath-KP against PD are, at least partially, achieved by preventing mitochondrial apoptosis.

Cath-KP attenuated oxidative stress in MN9D cells based on antioxidant activity

MPP$^+$ can induce mitochondrial ROS generation, leading to the accumulation of intracellular ROS and ultimately to neurotoxicity in DA neurons (Subramaniam & Chesselet, 2013). Therefore, the effects of Cath-KP on intracellular and mitochondrial ROS levels in MN9D cells were measured. As displayed in Figure 4A, D, green fluorescence intensity, reflecting intracellular ROS levels, was significantly increased after MPP$^+$ treatment. This elevation was significantly suppressed by the addition of Cath-KP. These findings were confirmed by representative flow cytometry analysis of ROS generation (Supplementary Figure S4A). In parallel, Cath-KP alleviated MPP$^+$-induced accumulation of mitochondrial ROS in MN9D cells (Figure 4B, E).

ROS generation is closely related to mitochondrial $\Delta\psi m$. A reduction in $\Delta\psi m$ is indicative of mitochondrial malfunction, under oxidative stress, and apoptosis. As shown in Figure 4C and F, prominent red fluorescence was observed in all cells, while green fluorescence was absent in the control cells and those treated with Cath-KP only. MPP$^+$ treatment led to a reduction in the red/green fluorescence ratio, indicating a decline in $\Delta\psi m$. Nevertheless, co-treatment with Cath-KP (5 µmol/L) effectively reversed this ratio. Similar findings were obtained by representative flow cytometry analysis of mitochondrial $\Delta\psi m$ (Supplementary Figure S4B). In accordance with its modulation of ROS levels, Cath-KP enhanced the activities of SOD and CAT, which function as cellular antioxidants, while diminishing the activity of NO, which inhibits complex I of the mitochondrial electron transport chain to facilitate ROS generation (Figure 4G–I) (Aquilano et al., 2008; Bloem et al., 2021).

In investigating the underlying mechanism for the antioxidant effects of Cath-KP in MPP$^+$-induced MN9D cells, the *in vitro* antioxidant activity of Cath-KP was further assessed. As shown in Figure 4J, K, Cath-KP was scavenged ABTS and DPPH radicals in a dose-dependent manner. Specifically, 40 µmol/L Cath-KP eliminated approximately 64.92% of ABTS radicals at 16 min and 26.47% of DPPH radicals at 9 min. Consistently, as shown in Figure 4L, the capacity of Cath-KP to reduce Fe^{3+} was improved with increasing concentration. Together, these findings indicate that Cath-KP exhibits antioxidant activity, diminishes ROS accumulation and its mitochondrial damage, and suppresses MPP$^+$-induced neuron death via inhibition of the mitochondrial apoptotic pathway.

Cath-KP modified the Sirt1/Nrf2 and FAK/p38-mediated pathways

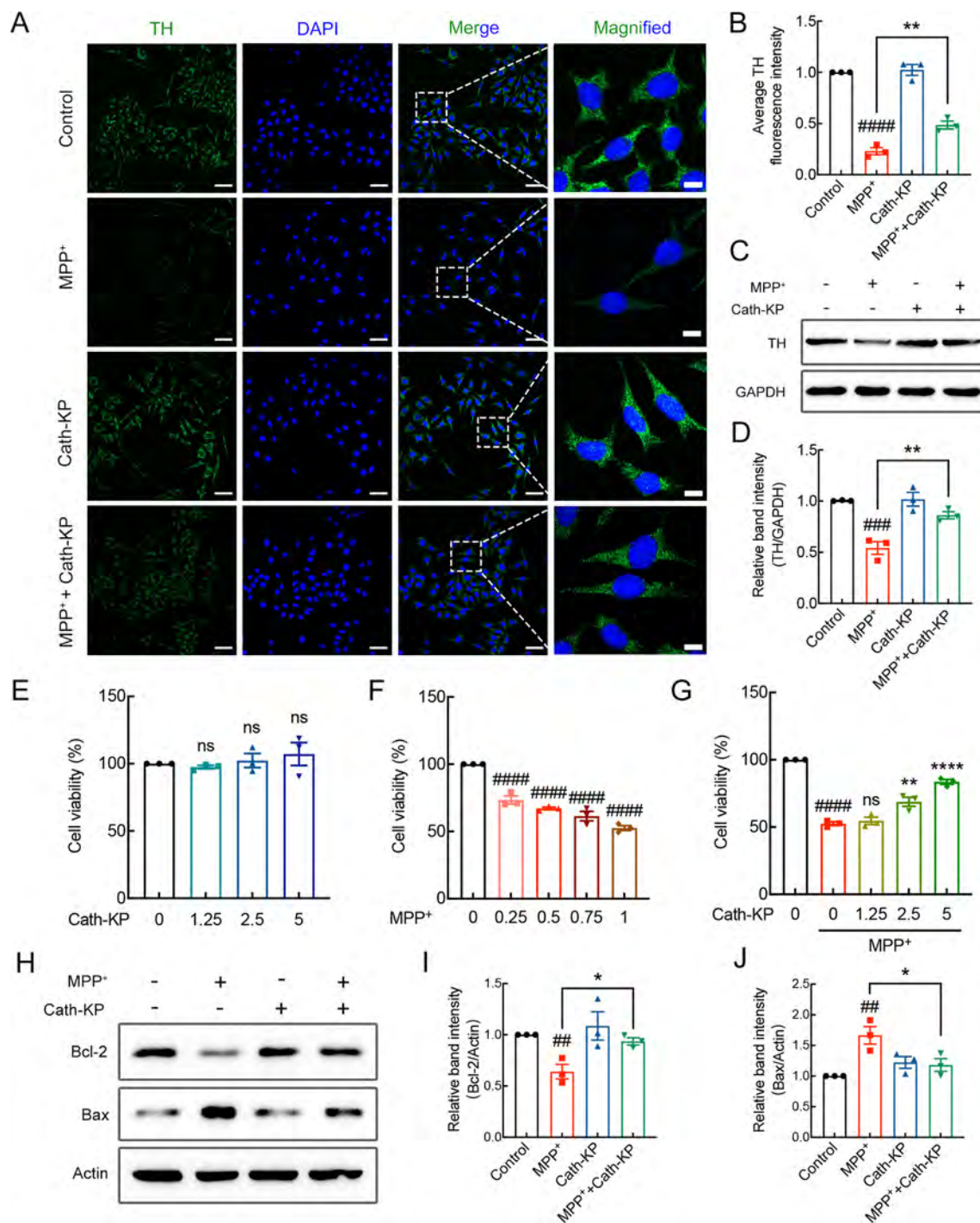The effects of Cath-KP on the Sirt1/Nrf2 pathway, which is

Figure 3 Cath-KP attenuated the decrease in tyrosine hydroxylase (TH) protein levels and reduced apoptosis of MPP⁺-treated MN9D cells

A, B: Example images from confocal laser scanning microscopy (A) and quantification of TH expression (B) in MN9D cells. MN9D cells were incubated with Cath-KP (5 μmol/L) for 24 h with MPP⁺ (1 mmol/L) present or absent before representative confocal laser scanning microscopy. TH, green fluorescence; DAPI, blue fluorescence. Scale bar: 50 μm for original and 10 μm for magnified images. C, D: Representative blots (C) and quantification analysis (D) of TH expression levels in MPP⁺ (1 mmol/L) and Cath-KP (5 μmol/L)-treated MN9D cells. E–G: Viability of MN9D cells treated with Cath-KP (0–5 μmol/L), MPP⁺ (0–1 mmol/L), J"and MPP⁺ (1 mmol/L) plus Cath-KP (0–5 μmol/L) for 24 h. H–J: Representative western blot images (H) and statistical analysis of Bcl-2 (I) and Bax (J) expression levels in MN9D cells. Data are represented as means±SEM with Student's t-test and ordinary one-way ANOVA (n=3). ns: Not significant. ##: $P<0.01$, ###: $P<0.001$, and ####: $P<0.0001$ vs. Control. *: $P<0.05$, **: $P<0.01$, and ****: $P<0.0001$ vs. PD models.

reported to control inflammatory reactions and redox homeostasis (Fão et al., 2019), were evaluated. As shown in Figure 5A, C, the expression levels of Sirt1, Keap1, Nrf2, SOD-1, SOD-2, and HO-1 in MN9D cells were markedly down-regulated by MPP⁺ treatment compared to the control group. In contrast, their expression levels were substantially

elevated by Cath-KP treatment compared to MPP⁺ treatment (Figure 5A, C). Notably, preincubation with the Sirt1-specific inhibitor EX527 (1 μmol/L) abolished the Cath-KP-enhanced expression levels of Sirt1, Nrf2, SOD-1, and SOD-2 in the MPP⁺-treated MN9D cells (Supplementary Figure S5). Consistently, as illustrated in Figure 5B, D, MPTP attenuated
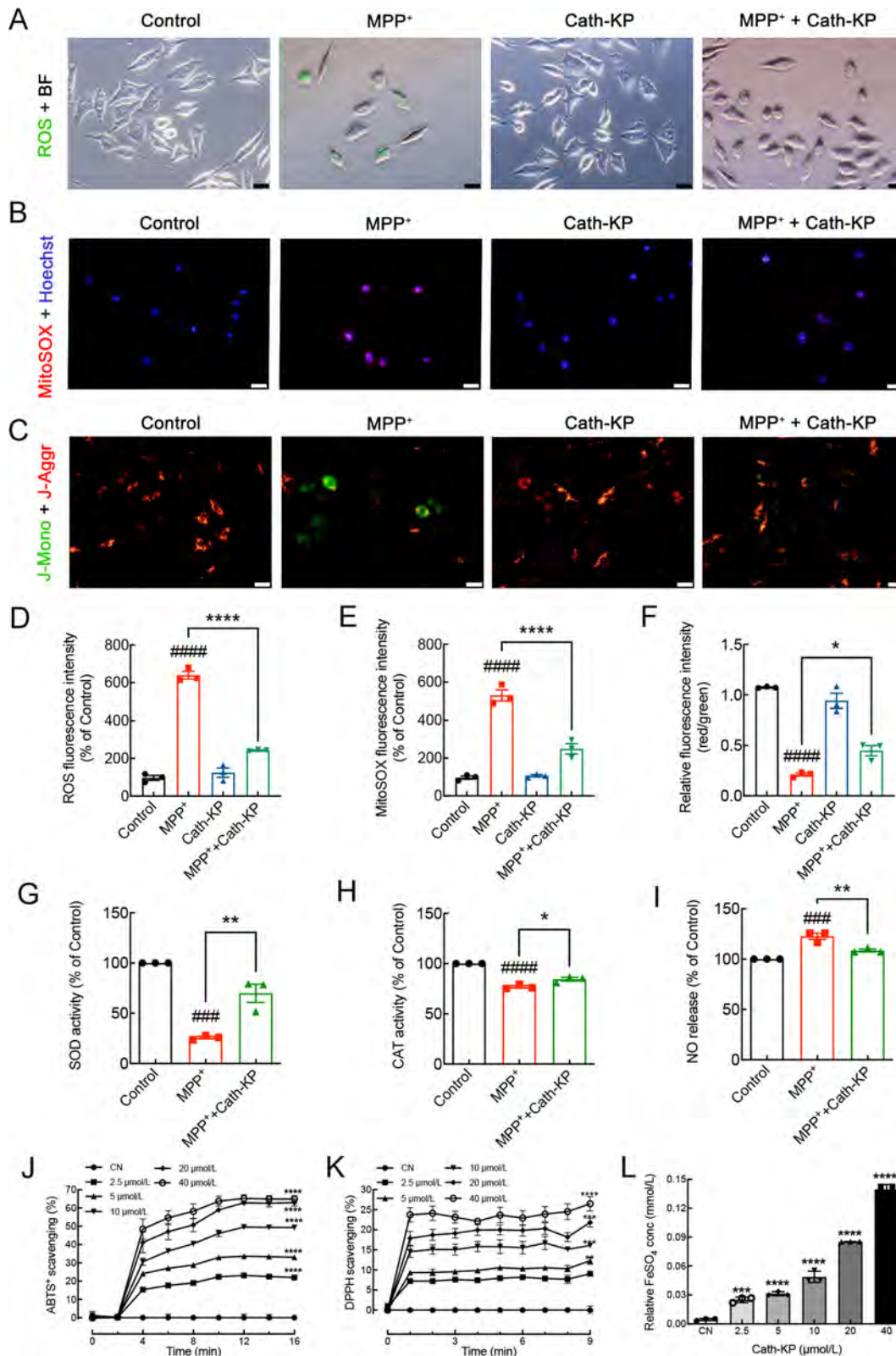
Figure 4 Cath-KP attenuated oxidative stress in MN9D cells based on its antioxidant activity

A, D: Representative fluorescence images (A) and quantitative analysis (D) of intracellular ROS generation in MPP⁺ and Cath-KP-treated MN9D cells. Intracellular ROS, green fluorescence; BF: Bright Field. Scale bar: 20 µm. B, E: Representative fluorescence images (B) and quantitative analysis (E) of mitochondrial ROS generation in MPP⁺ and Cath-KP-treated MN9D cells. Mitochondrial ROS, red fluorescence; Hoechst, blue fluorescence. Scale bar: 20 µm. C, F: Representative fluorescence images (C) and quantitative analysis (F) of mitochondrial $\Delta\psi m$ in MPP⁺ and Cath-KP-treated MN9D cells. J-Mono: J-Monomers, green fluorescence; J-Aggr: J-Aggregates, red fluorescence. Scale bar: 20 µm. G–I: Contents of SOD, CAT, and NO in MPP⁺ and Cath-KP-treated MN9D cells. J, K: ABTS and DPPH radical scavenging activity. L: FRAP antioxidant activity. Data are represented as means±SEM (n=3) with ordinary one-way ANOVA. ###: $P<0.001$ and ####: $P<0.0001$ vs. Control. *: $P<0.05$, **: $P<0.01$, ***: $P<0.001$, and ****: $P<0.0001$ vs. PD models.
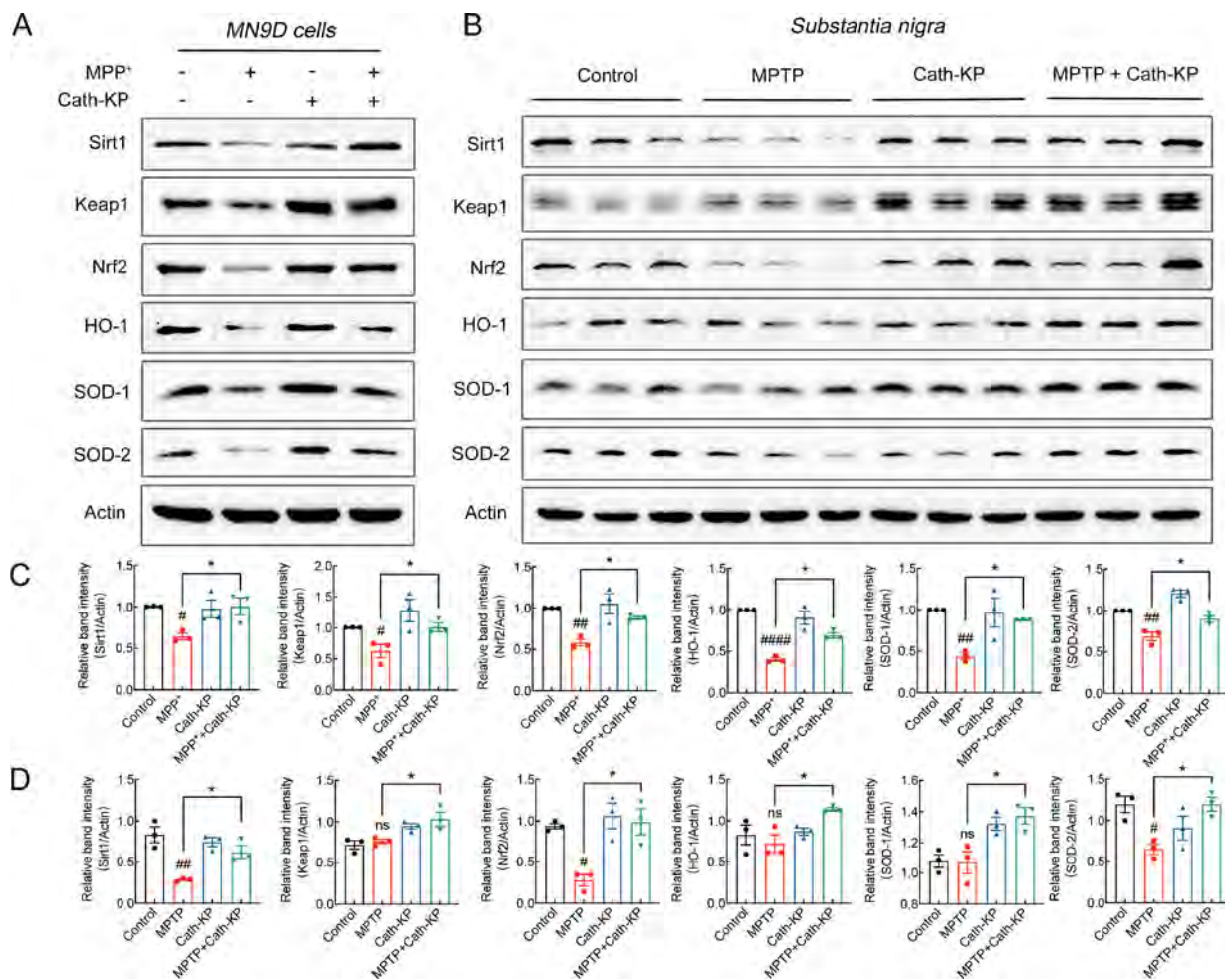
Figure 5 Modification of the Sirt1/Nrf2-mediated pathway by Cath-KP

A, C: Representative images (A) and quantification analysis (C) of western blots, detecting protein expression levels of Sirt1, Keap1, HO-1, Nrf2, SOD-1, and SOD-2 in MN9D cells incubated with MPP$^+$ and Cath-KP. B, D: Representative images (B) and quantification analysis (D) of western blots, detecting protein expression levels of Sirt1, Keap1, HO-1, Nrf2, SOD-1, and SOD-2 in mice treated with MPTP and Cath-KP. Data are represented as means±SEM (*n*=3) with ordinary one-way ANOVA. ns: Not significant. #: $P < 0.05$ and ##: $P < 0.01$ vs. Control. *: $P < 0.05$ vs. PD models.

the expression levels of Sirt1, Nrf2, SOD-2, and HO-1 in the SNpc of mice. These effects were reversed by Cath-KP co-treatment. Interestingly, the expression levels of Keap1 and SOD-1 were not changed under MPTP treatment but were significantly elevated in the peptide-treated group.

Research has indicated that ROS regulates the activation of p38 and FAK (Fão et al., 2019; Qin & Rodrigues, 2012). Therefore, we examined the potential impact of Cath-KP on the expression and phosphorylation of p38 and FAK in MPP$^+$-treated MN9D cells and in the SNpc of mice. As shown in Figure 6A, C, D, compared to the control, MPP$^+$ treatment markedly increased the phosphorylation of p38 but had no effect on its total protein expression. In contrast, MPP$^+$ treatment markedly decreased the phosphorylation of FAK, although also had no effect on its total protein level. However, the effects of MPP$^+$ on the phosphorylation of p38 and FAK were significantly mitigated by Cath-KP, aligning with observations in the SNpc of mice (Figure 6B, E, F).

Cath-KP promoted nuclear translocation of Nrf2

Typically, upon exposure to oxidative stress, Nrf2 undergoes translocation to the nucleus and interacts with antioxidant response elements (AREs), thus initiating the transcription of multiple antioxidant genes. Analysis of changes in red immunofluorescence intensity co-localized with blue DAPI revealed that MPP$^+$ treatment decreased nuclear Nrf2 levels and increased cytoplasmic Nrf2 levels (Figure 7A, C). Notably, these changes were reversed by Cath-KP treatment. Western blot analysis confirmed that MPP$^+$ treatment significantly decreased Nrf2 content in the nucleus while increasing its content in the cytoplasm, indicating suppression of nuclear translocation (Figure 7B, D). In contrast, Cath-KP enhanced the nuclear translocation of Nrf2 in the MPP$^+$-treated MN9D cells.

Cath-KP was cell-permeable and delivered to deep brain tissues

To ascertain the ability of Cath-KP to penetrate MN9D cells and exert antioxidant protection, the fluorescence emitted from FITC-Cath-KP incubated with MN9D cells was measured. Confocal microscopy (Figure 8A), with TH antibody fluorescence indicating cytoplasmic localization and DAPI fluorescence representing nuclear localization, revealed that FITC-Cath-KP effectively traversed the cytoplasmic membrane and entered the MN9D cells in a concentration-dependent manner relative to the control after 3 h of incubation (Figure 8A). Further examination was conducted to determine the influence of temperature on the internalization
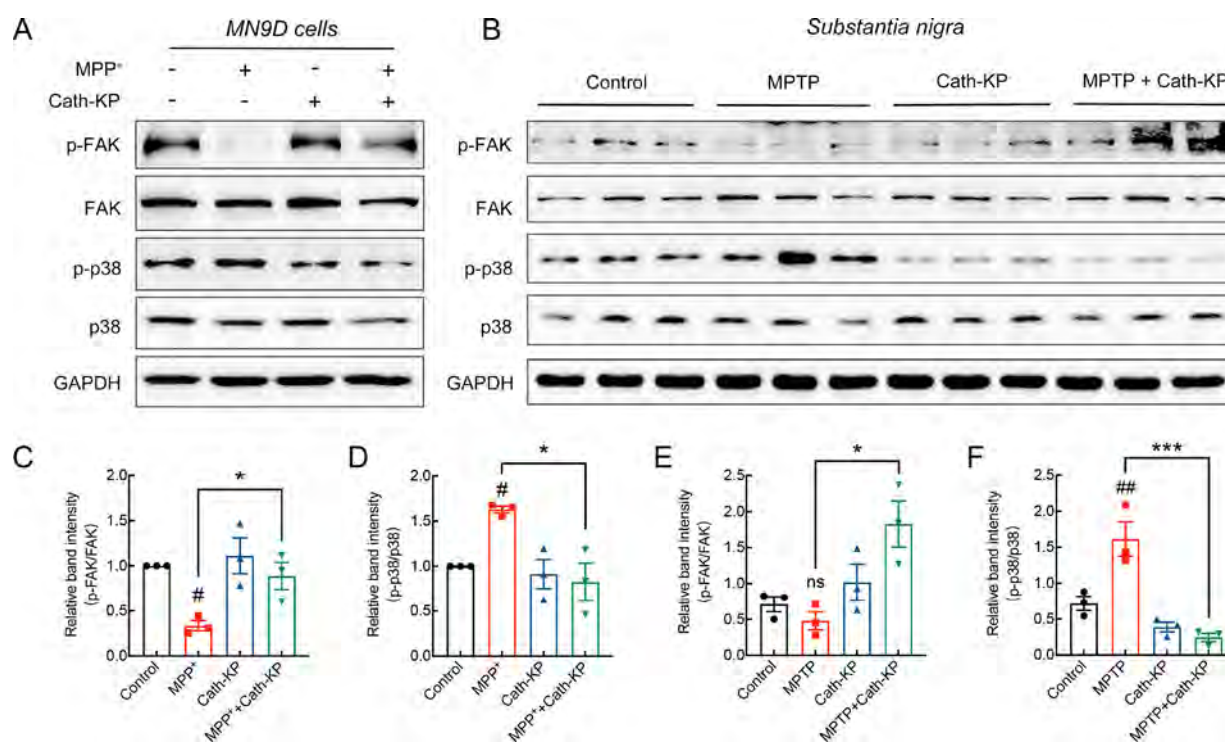
Figure 6 Modification of the FAK/p38-mediated pathway by Cath-KP

A, C, D: Representative images (A) and quantification analysis (C, D) of western blots, detecting protein expression levels of FAK and p38 in MN9D cells treated with MPP$^+$ and Cath-KP. B, E, F: Representative images (B) and quantification analysis (E, F) of western blots, detecting protein expression levels of FAK and p38 in mice treated with MPTP and Cath-KP. Data are represented as means±SEM (*n*=3) with ordinary one-way ANOVA. ns: Not significant. #: *P*<0.05 and ##: *P*<0.01 vs. Control. *: *P*<0.05 and ***: *P*<0.001 vs. PD models.

of FITC-Cath-KP. As shown in Figure 8B and Supplementary Figure S6A, B, FITC-Cath-KP entered the MN9D cells in a concentration-dependent manner. At 4 °C, cellular uptake was reduced by approximately 30% (2.5 μmol/L) and 39% (5 μmol/L) compared to uptake at 37 °C after 3 h of incubation, suggesting an energy-dependent and thermosensitive transport mechanism for Cath-KP across the MN9D cell membrane. Cell-penetrating peptides often first interact with heparin sulphate, a crucial component of cell membranes (Kim et al., 2015). Thus, we further examined whether heparin sulphate can affect FITC-Cath-KP absorption by cells. Compared to the FITC-Cath-KP only group, the internalization of FITC-Cath-KP was decreased by 39.38% after 30 min with 50 μg/mL heparin pretreatment (Figure 8B; Supplementary Figure S6C). Collectively, these findings suggest that Cath-KP may utilize endocytosis as its primary mechanism of entry into MN9D cells.

To evaluate the potential of Cath-KP to be delivered to brain tissue, brain sections were examined at 2 and 6 h following injections of diluent, FITC only, and FITC-Cath-KP. As shown in Figure 8C, FITC-Cath-KP was distributed into brain tissue and partially co-located with DA neurons, as evidenced by the green and red fluorescence from FITC-Cath-KP and TH antibody, respectively. Moreover, the fluorescence intensity of the FITC-Cath-KP samples at 2 h post-injection was higher than that at 6 h post-injection, indicating that Cath-KP can be non-selectively delivered to deep brain tissues within 2–6 h, with the peak at 2 h.

DISCUSSION

Amphibian skin plays a pivotal role in host defense and contains multiple bioactive peptides with antimicrobial, anti-

inflammatory, antitumor, and antioxidant properties (Xu & Lai, 2015). Among frogs belonging to the Microhylidae family, only a limited number of peptides have been identified, namely Brevinin-2KP and two trypsin inhibitors (Conlon & Kim, 2000; Gao et al., 2022; Zhang et al., 2010). In this study, we identified a novel peptide (Cath-KP) with antioxidant activity from the skin of *K. pulchra* frogs. Typically, frog skin bioactive peptide precursors contain an evolutionarily conserved N-terminal signal peptide, an acidic spacer region, and a C-terminal bioactive peptide, which undergo proteolytic cleavage at the KR or RR sites (Xu & Lai, 2015). The precursor of Cath-KP also exhibited this structure. Thus, the sequence following the cathelin domain, ending at the basic RR residues (GCSGRFCNLFNNRRPGRLTLIHRPGGDKRTSTGLIYV), was considered the mature peptide and a new member of the cathelicidin family. Most antimicrobial cathelicidins, including Cath-MH, cathelicidin-PY, and LL-37, contain high amphipathic *α*- helices in membrane-mimetic environments (Chai et al., 2021; Sancho- Vaello et al., 2017; Wei et al., 2013). In contrast, secondary structure modeling, helix-wheel analysis, and CD spectra results demonstrated that Cath-KP lacked this feature, despite its high net charge of 6 at neutral pH (Figure 1C; Supplementary Figure S7), causing the loss of antimicrobial activity (data not shown). Critical residues such as leucine, proline, phenylalanine, tyrosine, methionine, tryptophan, and free cysteine, capable of donating protons to radicals with low electron density, underpin the functionality of amphibian antioxidant peptides (Chai et al., 2022; Guo et al., 2014; Krishnan et al., 2008; Yang et al., 2009; Zeng et al., 2020a). Here, the primary sequence of Cath-KP consisted of eight hydrophobic amino acids, including four leucine residues, two proline residues, one phenylalanine residue, and one tyrosine residue (Figure 1A). Thus, we hypothesized that
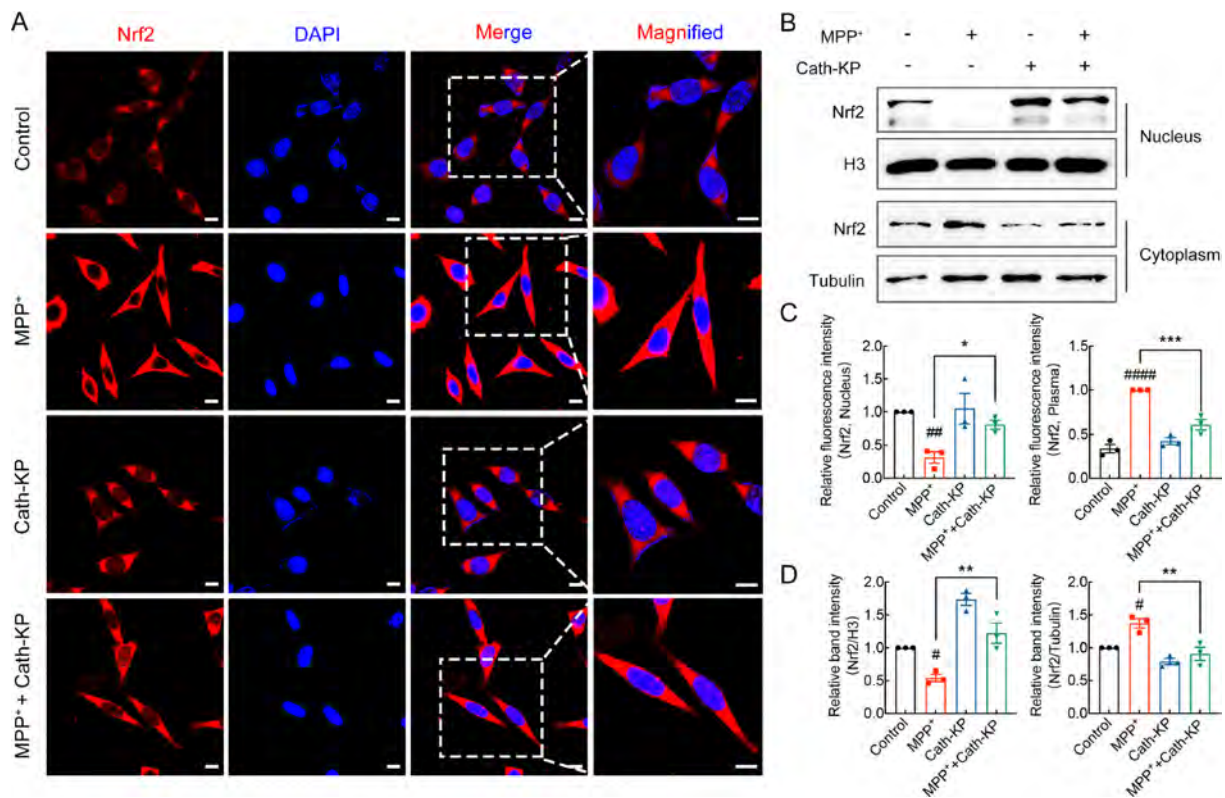
Figure 7 Nuclear translocation of Nrf2 by Cath-KP

A–D: Immunofluorescent staining (A), western blot analysis (B), and quantification (C, D) showing nuclear translocation of Nrf2 in MN9D cells. Nrf2, red fluorescence; DAPI, blue fluorescence. Scale bar: 10 μm for original images and 5 μm for magnified images in (A). Data are represented as means±SEM (*n*=3) with ordinary one-way ANOVA. [#]: *P*<0.05, [##]: *P*<0.01, and [####]: *P*<0.0001 vs. Control. [*]: *P*<0.05, [**]: *P*<0.01, and [***]: *P*<0.001 vs. PD models.

Cath-KP possessed antioxidant activity, as confirmed by ABTS, DPPH, and FRAP assays and oxidative stress measurement in MPP[+]-treated cells (Figure 4; Supplementary Figure S4). Interestingly, prolonged exposure to sunlight and strong ultraviolet radiation may contribute to the development and production of antioxidant peptides in amphibians (Guo et al., 2014; Yang et al., 2009). We previously discovered an antioxidant peptide from *Fejervarya limnocharis* , a frog species that shares the same habitat as *K. pulchra* in tropical solar radiation-exposed Guangdong Province in a low-elevation region (N23.12°, E113.28°) (Chai et al., 2022). Therefore, our results provide further evidence that the development of antioxidant peptides is linked to ultraviolet exposure and the presence of antioxidant peptides reflects the adaptation of frog species to a specific environment (Chai et al., 2022; Guo et al., 2014; Liu et al., 2010; Yang et al., 2016).

MPTP/MPP[+] models have been widely used to assess pathology, pharmacology, and drug metabolism in PD (Dauer & Przedborski, 2003; Zhang et al., 2017). In this research, MPP[+]-stimulated MN9D cells and MPTP-induced mice were used as PD models to explore the neuroprotective effects of Cath-KP *in vitro* and *in vivo*. Consistent with previous findings that MPP[+] can damage proteins, lipids, and mitochondria, consequently altering the status of brain antioxidant enzymes (Dauer & Przedborski, 2003; Zhang et al., 2017) and inducing Parkinsonian syndrome and behavioral deficits (Tillerson et al., 2002; Watanabe et al., 2008), our results showed a remarkable decrease in MPP[+]-induced MN9D cell viability, paralleling a decrease in mitochondrial *Δψm* and increase in intracellular and mitochondrial ROS levels (Figures 3E–G,

4A–F). Results also showed a concurrent decrease in the levels of antioxidant enzymes, including SOD and CAT (Figure 4G–I). Motor deficits and cognitive impairments in the MPTP-induced PD mice were also observed, as shown by the rotarod, open field, grasping, and pole-climbing tests (Figure 2B–H), which are widely used to assess balance and motor coordination, exploratory activity, locomotor activity, learning and memory ability, and movement disorders related to the basal ganglia (Dauer & Przedborski, 2003; Tillerson et al., 2002; Watanabe et al., 2008; Zhang et al., 2017). Consistent with its antioxidant effects, as shown by the ABTS and DPPH radical scavenging and FRAP antioxidant assays, Cath-KP increased antioxidant enzymes, attenuated intracellular and mitochondrial ROS and total NO accumulation, protected mitochondria, and reversed toxic effects in MPP[+]-induced MN9D cells (Figures 3, 4). In addition, Cath-KP restored the antioxidant enzyme levels in the mouse brain tissues (Figure 5B, D), reduced oxidative damage from MPTP insult (Figure 2I–P), and improved mouse performance in the behavior tests (Figure 2B–H). Overall, these results demonstrate that Cath-KP can prevent PD damage by enhancing cell survival and reducing oxidative stress due to its antioxidant functions.

DA neurons in the SNpc and striatum diminish over time, resulting in motor impairments, which are the hallmark of PD. The TH enzyme is essential in dopamine production and phenotypic expression (Daubner et al., 2011). Motor function impairment induced by MPTP in PD animal models is typically accompanied by a marked reduction in TH-positive cells in the SNpc (Moreira et al., 2010). Similarly, in the current study, MPTP injection lowered TH content and TH-positive neurons
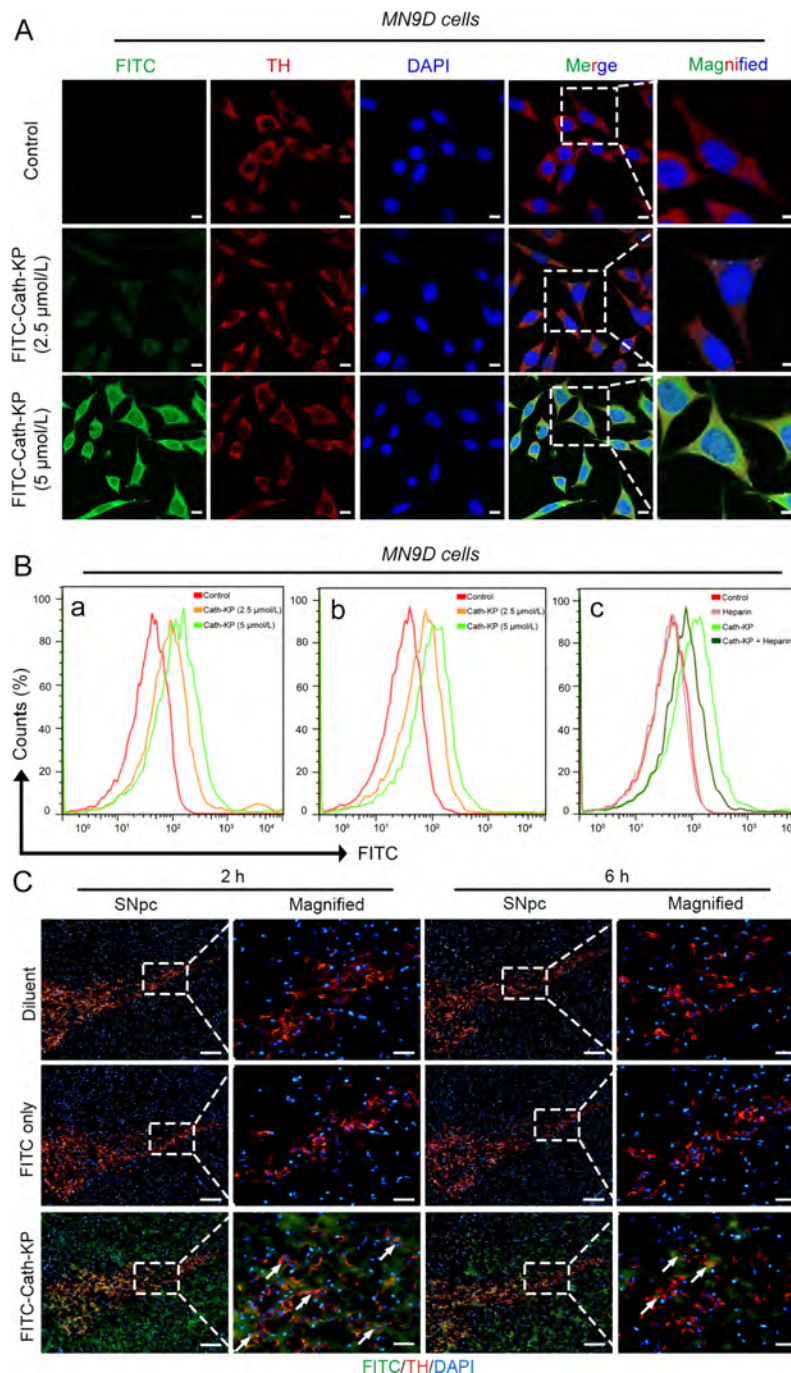
Figure 8 Internalization of Cath-KP into MN9D cells and brain tissue

A: Representative confocal laser scanning microscopy images of FITC-Cath-KP entering MN9D cells. FITC-Cath-KP, green fluorescence; TH, red fluorescence; DAPI, blue fluorescence. Scale bar: 10 μm for original images and 5 μm for magnified images in white square. B: Representative flow cytometry analysis of FITC-Cath-KP entry into MN9D cells under different conditions. Cath-KP (2.5 and 5 μmol/L) was incubated with MN9D cells for 3 h at 37 °C (panel a), 4 °C (panel b), or in the presence of 50 μg/mL heparin (panel c). Fluorescence intensity was then measured by flow cytometry. C: Characteristic TH staining images of SNpc from mice at 2 and 6 h after diluent, FITC only, and FITC-Cath-KP injections. FITC-Cath-KP, green fluorescence; TH, red fluorescence; DAPI, blue fluorescence. White arrows in enlarged area of the right column show the presence of FITC-Cath-KP in DA neurons. Scale bars=100 μm for original images and 20 μm for magnified images.

in the striatum and SNpc (Figure 2I–M). Interestingly, Cath-KP significantly reversed these changes in both the striatum and MN9D cells (Figures 2I–M, 3A–G). Multiple cell death pathways exist, including apoptosis, cell necrosis, and ferroptosis (Callizot et al., 2019; Tang et al., 2023). Endogenous apoptosis (also known as mitochondrial apoptosis), which greatly affects PD pathophysiology, can be triggered by excessive ROS accumulation (Radi et al., 2014).

Apoptosis-induced cell death has been demonstrated in PD models *in vivo* (Radi et al., 2014). In line with these studies, our results further demonstrated that apoptosis in MN9D cells and the SNpc was substantially enhanced by MPP[+]/MPTP exposure but was inhibited in the presence of Cath-KP, as evidenced by the increasing Bcl-2/Bax ratio (Figures 2N–P, 3H–J), a key factor regulating cell apoptosis (Bar-Am et al., 2005). Thus, the protective effects of Cath-KP on DA neurons

may be associated with its suppression of the mitochondrial apoptotic pathway.

The Sirt1/Nrf2 pathway regulated both inflammatory response and redox homeostasis (Fão et al., 2019). Brain-specific deletion of Sirt1 significantly increases ROS levels, exacerbating mitochondrial dysregulation and promoting cell death. The SNpc experiences more severe DA cell loss in the absence of Nrf2 because Nrf2 activation can up-regulate the expression of antioxidant enzymes/proteins like SOD, HO-1, and glutathione S-transferase, offering protection against oxidative stress (Wang et al., 2018). Consistent with previous research (Dong et al., 2016; Wang et al., 2018), our study showed that MPTP/MPP$^+$ treatment markedly decreased Sirt1 protein levels. Notably, Cath-KP administration reversed this decrease and subsequently increased the expression and nuclear location of Nrf2 and its downstream effectors (SOD, HO-1, and CAT) in both MN9D cells and brain tissue, thus protecting against MPP$^+$-induced oxidative damage (Figures 4G–I, 5, 7). Additionally, the effects of Cath-KP were suppressed by the Sirt1-specific inhibitor EX527 (Supplementary Figure S5). These findings suggest that the Sirt1/Nrf2 antioxidant pathway plays an essential role in the neuroprotective effects of Cath-KP in PD.

Nrf2 dissociates from its negative modulator Keap1 in the cytosol, translocates into the nucleus, and binds to AREs, thus promoting the transcription of antioxidant proteins (Fão et al., 2019). Here, compared to the control group, Keap1 expression decreased in the MN9D cells treated with MPP$^+$ but not significantly in the MPTP-treated tissues (Figure 5). Previous studies have reported that the protein level of Keap1 can be significantly decreased in endothelial cells by H_2O_2 and MPP$^+$ stimulation (Guo et al., 2021; Zhu et al., 2019), similar to our MN9D cell results. Studies have also shown that irigenin can suppress Keap1 expression, with GABA treatment partially rescuing this decrease (Guo et al., 2021; Zhu et al., 2019), correlating well with our cell experiments (Figure 5). Interestingly, research has also reported that SAP can reduce Keap1 expression in mice, which can be reversed by the antioxidant sitagliptin via Keap1/Nrf2 signaling pathway activation (Kong et al., 2021). However, oxidative stress does not modify the expression of Keap1 in H9c2 cells (Yao et al., 2022); as such, oxidative stress may induce different effects on the Keap1 protein, which warrants further study. Of note, changes in Keap1 expression do not appear to affect Nrf2 expression or its downstream antioxidant molecules, such as SOD and HO-1 (Bian et al., 2021; Choi et al., 2018; Guo et al., 2021; Kong et al., 2021; Pan et al., 2022; Yao et al., 2022; Zhu et al., 2019). In accordance with this conclusion, the expression patterns of other signaling proteins from cells and brain tissues remained consistent, even with variations in Keap1 expression, when compared to the MPTP/MPP$^+$ treatment groups (Figure 5).

Accumulating evidence suggests that overexpression of Sirt1 can inhibit p38 activation, leading to elevated SOD-1 and Bcl-2 expression, and reduced neuronal and inducible NO synthases governing NO generation (Aquilano et al., 2008; Bloem et al., 2021; Fão et al., 2019; Wang et al., 2018). In addition, p38 may phosphorylate Nrf2, facilitating its association with Keap1 and inhibiting its nuclear translocation (Fão et al., 2019; Karunakaran & Ravindranath, 2009; Newhouse et al., 2004). Thus, various antioxidants, including xanthohumol, ethanol extract of *Centipeda minima* (ECM), eriodictyol, salidroside, and anthocyanin loaded nanoparticles

(An-NPs), can exert antioxidant and neuroprotective effects by activating the Nrf2 pathway while dephosphorylating p38 in different cells and animal models (Amin et al., 2017; Fão et al., 2019; Jiao et al., 2020; Jing et al., 2015; Wang et al., 2018, 2019). Consistently, Cath-KP mitigated MPP$^+$-induced p38 activation (Figure 6). The intracellular tyrosine kinase FAK is thought to control a variety of cellular processes, including cell adhesion, migration, invasion, polarity, proliferation, and survival (Parsons, 2003). MPP$^+$ treatment in SH-SY5Y cells inhibits FAK phosphorylation, while luteolin, which possesses antioxidative properties, stabilizes phosphorylated FAK levels and exhibits neuroprotective effects (Reudhabibadh et al., 2021). In addition, maclurin, which shows pro-oxidant activity, can activate p38 signaling and inhibit c-JNK, FAK, AKT, and c-Myc signaling in PC3 cells (Lee et al., 2018). Similarly, our results showed that Cath-KP inhibited p38 phosphorylation and induced further suppression of FAK phosphorylation induced by MPTP/MPP$^+$ treatment (Figure 6). Previous research has indicated that Sirt1/FAK regulates the nuclear translocation of p65 via phosphorylation of p38 (Grbčić et al., 2017; Karunakaran & Ravindranath, 2009; Wan et al., 2019). Thus, Cath-KP likely exerts its neuroprotective effects on PD models by activating the Sirt1/Nrf2 pathway, promoting the expression of antioxidant enzymes, and inhibiting the mitochondrial apoptotic pathway. Furthermore, FAK and p38 appear to be involved in the regulation of this pathway, although the exact regulatory mechanism requires further elucidation.

The BBB impedes the delivery of many therapeutic agents to the central nervous system, complicating treatment approaches for many neurological disorders (Guidotti et al., 2017). In our study, Cath-KP showed potential properties for cell penetration and BBB traversal (Figure 8). According to conventional wisdom, under physiological pH conditions, the guanidine head group of arginine can form bidentate hydrogen bonds with the negatively charged sulphate, carboxylic, and phosphate groups on cell membranes, resulting in cellular internalization of cell-penetrating peptides (Guidotti et al., 2017; Rothbard et al., 2004). Therefore, the transduction capabilities of cell-penetrating peptides can be greatly influenced by the amount and order of amino acids in their sequences, especially arginine. Consistently, Cath-KP contained six arginine residues and heparin sulfate suppressed its cellular uptake (Figures 1A, 8B). Moreover, its cellular internalization was energy-dependent, as evidenced by the decreased uptake rate at 4 °C than at 37 °C (Figure 8B). Thus, the cellular internalization mechanism of Cath-KP functions via energy-dependent endocytosis rather than energy-independent direct penetration. The primary sequence of Cath-KP contained an RTS motif, which is frequently found in disintegrins targeting $α_1β_1$ integrin (Calvete et al., 2007). In the mammalian central nervous system, $α_1β_1$ integrin is expressed in astrocytes and endothelial cells and plays an important role in maintaining the physiological integrity and stability of the BBB (Peng et al., 2008; Yonezawa et al., 2010). Our molecular docking and antibody competent assays showed that Cath-KP can bind to $α_1β_1$ integrin (Supplementary Figures S8, S9). Consequently, we cannot rule out the possibility that the direct translocation of Cath-KP across the BBB is related to its effects on $α_1β_1$ integrin in astrocytes. Therefore, more detailed research is required to further explore its uptake process. Nevertheless, the cellular uptake of Cath-KP highlights its value as a drug candidate for

PD therapy. Furthermore, given the role of non-human primates in the development of therapeutics for human diseases (Lei et al., 2015; Li et al., 2021a, 2021b; Su et al., 2015), evaluating the effects of Cath-KP in non-human primate models of PD is essential.

In conclusion, we identified a novel antioxidant peptide (Cath-KP) belonging to the cathelicidin family from the skin of *K. pulchra*. Our results showed that Cath-KP alleviated dyskinesia in MPTP mice by reversing DA neuron loss in the SNpc and decreasing TH levels in the striatum. Mechanistically, Cath-KP penetrated cells and exerted a neuroprotective effect via Sirt1/Nrf2 pathway modulation, further promoting the expression of antioxidant enzymes and alleviating the accumulation of ROS. Additionally, FAK and p38 contributed to this regulatory process. These findings demonstrate the potential of Cath-KP as a therapeutic option for PD that targets oxidative stress.

DATA AVAILABILITY

The raw RNA-seq data were deposited in the NCBI Sequence Read Archive (SRA)(BioProjectID PRJNA1021395), GSA Database (Accession No. CRA013484), and Science Data Bank (https://doi.org/10.57760/sciencedb.j00139.00068).

SUPPLEMENTARY DATA

Supplementary data to this article can be found online.

COMPETING INTERESTS

The authors declare that they have no competing interests.

AUTHORS' CONTRIBUTIONS

H.L. and J.C. performed the major experiments, organized the data, and wrote the original manuscript. S.Q. and X.X. designed the experiments, supervised the study, evaluated the data, and revised the article. Z.X. performed molecular docking. J.W., S.H., H.L., P.H., and X.C. carried out the experiments. X.H. and H.J. revised the manuscript. All authors read and approved the final version of the manuscript.

REFERENCES

Amin FU, Shah SA, Badshah H, et al. 2017. Anthocyanins encapsulated by PLGA@PEG nanoparticles potentially improved its free radical scavenging capabilities via p38/JNK pathway against $A\beta_{1-42}$-induced oxidative stress. *Journal of Nanobiotechnology*, **15**(1): 12.

Aquilano K, Baldelli S, Rotilio G, et al. 2008. Role of nitric oxide synthases in Parkinson's disease: a review on the antioxidant and anti-inflammatory activity of polyphenols. *Neurochemical Research*, **33**(12): 2416−2426.

Bar-Am O, Weinreb O, Amit T, et al. 2005. Regulation of Bcl-2 family proteins, neurotrophic factors, and APP processing in the neurorescue activity of propargylamine. *The FASEB Journal*, **19**(13): 1899−1901.

Bian YQ, Chen Y, Wang XF, et al. 2021. Oxyphylla A ameliorates cognitive deficits and alleviates neuropathology via the Akt-GSK3β and Nrf2-Keap1-HO-1 pathways in *vitro* and in *vivo* murine models of Alzheimer's disease. *Journal of Advanced Research*, **34**: 1−12.

Bloem BR, Okun MS, Klein C. 2021. Parkinson's disease. *The Lancet*, **397**(10291): 2284−2303.

Callizot N, Combes M, Henriques A, et al. 2019. Necrosis, apoptosis, necroptosis, three modes of action of dopaminergic neuron neurotoxins. *PLoS One*, **14**(4): e0215277.

Calvete JJ, Marcinkiewicz C, Sanz L. 2007. KTS and RTS-disintegrins: anti-angiogenic viper venom peptides specifically targeting the α1β1 integrin. *Current Pharmaceutical Design*, **13**(28): 2853−2859.

Cao XQ, Wang Y, Wu CY, et al. 2018. Cathelicidin-OA1, a novel antioxidant peptide identified from an amphibian, accelerates skin wound healing. *Scientific Reports*, **8**(1): 943.

Chai JW, Chen X, Ye TF, et al. 2021. Characterization and functional analysis of cathelicidin-MH, a novel frog-derived peptide with anti-septicemic properties. *eLife*, **10**: e64411.

Chai JW, Liu JF, Tian ML, et al. 2022. Multiple mechanistic action of Brevinin-1FL peptide against oxidative stress effects in an acute inflammatory model of carrageenan-induced damage. *Oxidative Medicine and Cellular Longevity*, **2022**: 2615178.

Choi JH, Jang M, Lee JI, et al. 2018. Neuroprotective effects of a traditional multi-herbal medicine Kyung-Ok-Ko in an animal model of Parkinson's disease: inhibition of MAPKs and NF-κB pathways and activation of Keap1-Nrf2 pathway. *Frontiers in Pharmacology*, **9**: 1444.

Conlon JM, Kim JB. 2000. A protease inhibitor of the Kunitz family from skin secretions of the tomato frog, *Dyscophus guineti* (Microhylidae). *Biochemical and Biophysical Research Communications*, **279**(3): 961−964.

Daubner SC, Le T, Wang SZ. 2011. Tyrosine hydroxylase and regulation of dopamine synthesis. *Archives of Biochemistry and Biophysics*, **508**(1): 1−12.

Dauer W, Przedborski S. 2003. Parkinson's disease: mechanisms and models. *Neuron*, **39**(6): 889−909.

Dong SY, Guo YJ, Feng Y, et al. 2016. The epigenetic regulation of HIF-1α by SIRT1 in MPP^+ treated SH-SY5Y cells. *Biochemical and Biophysical Research Communications*, **470**(2): 453−459.

Dorsey ER, Constantinescu R, Thompson JP, et al. 2007. Projected number of people with Parkinson disease in the most populous nations, 2005 through 2030. *Neurology*, **68**(5): 384−386.

Eiríksdóttir E, Konate K, Langel Ü, et al. 2010. Secondary structure of cell-penetrating peptides controls membrane interaction and insertion. *Biochimica et Biophysica Acta*, **1798**(6): 1119−1128.

Fão L, Mota SI, Rego AC. 2019. Shaping the Nrf2-ARE-related pathways in Alzheimer's and Parkinson's diseases. *Ageing Research Reviews*, **54**: 100942.

Fauna CGOCMA. 1983. China Medicinal Animal Fauna. Tianjin: Tianjin Science and Technology Press. (in Chinese)

Fei L, Ye CY, Jiang JP. 2012. Colored Atlas of Chinese Amphibians and Their Distributions. Chengdu: Sichuan Science and Technology Press. (in Chinese)

Feng GZ, Wei L, Che HL, et al. 2022. Cathelicidin-NV from *Nanorana ventripunctata* effectively protects HaCaT cells, ameliorating ultraviolet B-induced skin photoaging. *Peptides*, **150**: 170712.

Gao YH, Chai JW, Wu JN, et al. 2022. Molecular cloning and characterization of a novel antimicrobial peptide from the skin of *Kaloula pulchra*. *Current Pharmaceutical Biotechnology*, **23**(15): 1873–1882.

Grbčić P, Tomljanović I, Klobučar M, et al. 2017. Dual sphingosine kinase inhibitor SKI-II enhances sensitivity to 5-fluorouracil in hepatocellular carcinoma cells via suppression of osteopontin and FAK/IGF-1R signalling. *Biochemical and Biophysical Research Communications*, **487**(4): 782−788.

Guidotti G, Brambilla L, Rossi D. 2017. Cell-penetrating peptides: from basic research to clinics. *Trends in Pharmacological Sciences*, **38**(4): 406−424.

Guo C, Hu YH, Li J, et al. 2014. Identification of multiple peptides with antioxidant and antimicrobial activities from skin and its secretions of *Hylarana taipehensis*, *Amolops lifanensis* , and *Amolops granulosus*. *Biochimie*, **105**: 192–201.

Guo F, Wang XX, Liu XX. 2021. Protective effects of irigenin against 1-methyl-4-phenylpyridinium-induced neurotoxicity through regulating the Keap1/Nrf2 pathway. *Phytotherapy Research*, **35**(3): 1585−1596.

Hao X, Yang HL, Wei L, et al. 2012. Amphibian cathelicidin fills the evolutionary gap of cathelicidin in vertebrate. *Amino Acids*, **43**(2): 677−685.

Jiao Y, Cao YZ, Lu XY, et al. 2020. Xanthohumol protects neuron from cerebral ischemia injury in experimental stroke. *Molecular Biology Reports*,

47(4): 2417−2425.

Jing X, Shi HY, Zhu XY, et al. 2015. Eriodictyol attenuates β-amyloid 25–35 peptide-induced oxidative cell death in primary cultured neurons by activation of Nrf2. *Neurochemical Research*, **40**(7): 1463−1471.

Karunakaran S, Ravindranath V. 2009. Activation of p38 MAPK in the substantia nigra leads to nuclear translocation of NF-κB in MPTP-treated mice: implication in Parkinson's disease. *Journal of Neurochemistry*, **109**(6): 1791−1799.

Kim HY, Yum SY, Jang G, et al. 2015. Discovery of a non-cationic cell penetrating peptide derived from membrane-interacting human proteins and its potential as a protein delivery carrier. *Scientific Reports*, **5**: 11719.

Kong LM, Deng J, Zhou X, et al. 2021. Sitagliptin activates the p62-Keap1-Nrf2 signalling pathway to alleviate oxidative stress and excessive autophagy in severe acute pancreatitis-related acute lung injury. *Cell Death & Disease*, **12**(10): 928.

Krishnan N, Dickman MB, Becker DF. 2008. Proline modulates the intracellular redox environment and protects mammalian cells against oxidative stress. *Free Radical Biology and Medicine*, **44**(4): 671−681.

Lee YJ, Jung O, Lee J, et al. 2018. Maclurin exerts anti-cancer effects on PC3 human prostate cancer cells via activation of p38 and inhibitions of JNK, FAK, AKT, and c-Myc signaling pathways. *Nutrition Research*, **58**: 62−71.

Lei XG, Li H, Huang BH, et al. 2015. 1-Methyl-4-phenylpyridinium stereotactic infusion completely and specifically ablated the nigrostriatal dopaminergic pathway in rhesus macaque. *PLoS One*, **10**(5): e0127953.

Li H, Su LY, Yang LX, et al. 2021a. A cynomolgus monkey with naturally occurring Parkinson's disease. *National Science Review*, **8**(3): nwaa292.

Li H, Yao YG, Hu XT. 2021b. Biological implications and limitations of a cynomolgus monkey with naturally occurring Parkinson's disease. *Zoological Research*, **42**(2): 138−140.

Li K, Wang M, Huang ZH, et al. 2023. ALOX5 inhibition protects against dopaminergic neurons undergoing ferroptosis. *Pharmacological Research*, **193**: 106779.

Liu CB, Hong J, Yang HL, et al. 2010. Frog skins keep redox homeostasis by antioxidant peptides with rapid radical scavenging ability. *Free Radical Biology and Medicine*, **48**(9): 1173−1181.

Moreira ELG, Rial D, Aguiar Jr AS, et al. 2010. Proanthocyanidin-rich fraction from *Croton celtidifolius* Baill confers neuroprotection in the intranasal 1-methyl-4-phenyl-1, 2, 3, 6-tetrahydropyridine rat model of Parkinson's disease. *Journal of Neural Transmission*, **117**(12): 1337−1351.

Mwangi J, Hao X, Lai R, et al. 2019. Antimicrobial peptides: new hope in the war against multidrug resistance. *Zoological Research*, **40**(6): 488−505.

Newhouse K, Hsuan SL, Chang SH, et al. 2004. Rotenone-induced apoptosis is mediated by p38 and JNK MAP kinases in human dopaminergic SH-SY5Y cells. *Toxicological Sciences*, **79**(1): 137−146.

Pan SP, Wei HM, Yuan SS, et al. 2022. Probiotic *Pediococcus pentosaceus* ameliorates MPTP-induced oxidative stress *via* regulating the gut microbiota-gut-brain axis. *Frontiers in Cellular and Infection Microbiology*, **12**: 1022879.

Parsons JT. 2003. Focal adhesion kinase: the first ten years. *Journal of Cell Science*, **116**(8): 1409−1416.

Peng HS, Shah W, Holland P, et al. 2008. Integrins and dystroglycan regulate astrocyte wound healing: the integrin β1 subunit is necessary for process extension and orienting the microtubular network. *Developmental Neurobiology*, **68**(5): 559−574.

Qi RH, Chen Y, Guo ZL, et al. 2019. Identification and characterization of two novel cathelicidins from the frog *Odorrana livida*. *Zoological Research*, **40**(2): 94−101.

Qin SF, Rodrigues GA. 2012. Roles of αvβ5, FAK and MerTK in oxidative stress inhibition of RPE cell phagocytosis. *Experimental Eye Research*, **94**(1): 63−70.

Qu LL, Lin BQ, Zeng WP, et al. 2022. Lysosomal K$^+$ channel TMEM175 promotes apoptosis and aggravates symptoms of Parkinson's disease. *EMBO Reports*, **23**(9): e53234.

Radi E, Formichi P, Battisti C, et al. 2014. Apoptosis and oxidative stress in neurodegenerative diseases. *Journal of Alzheimer's Disease*, **42 Suppl 3**: S125–S152.

Reudhabibadh R, Binlateh T, Chonpathompikunlert P, et al. 2021. Suppressing Cdk5 activity by luteolin inhibits MPP$^+$-induced apoptotic of neuroblastoma through ERK/DRP1 and FAK/Akt/GSK3β pathways. *Molecules*, **26**(5): 1307.

Rothbard JB, Jessop TC, Lewis RS, et al. 2004. Role of membrane potential and hydrogen bonding in the mechanism of translocation of guanidinium-rich peptides into cells. *Journal of the American Chemical Society*, **126**(31): 9506−9507.

Sancho-Vaello E, François P, Bonetti EJ, et al. 2017. Structural remodeling and oligomerization of human cathelicidin on membranes suggest fibril-like structures as active species. *Scientific Reports*, **7**(1): 15371.

Su LY, Li H, Lv L, et al. 2015. Melatonin attenuates MPTP-induced neurotoxicity via preventing CDK5-mediated autophagy and SNCA/α-synuclein aggregation. *Autophagy*, **11**(10): 1745−1759.

Subramaniam SR, Chesselet MF. 2013. Mitochondrial dysfunction and oxidative stress in Parkinson's disease. *Progress in Neurobiology*, **106–107**: 17–32.

Tang F, Zhou LY, Li P, et al. 2023. Inhibition of ACSL4 alleviates parkinsonism phenotypes by reduction of lipid reactive oxygen species. *Neurotherapeutics*,doi: 10.1007/s13311-023-01382-4.

Tatton WG, Chalmers-Redman R, Brown D, et al. 2003. Apoptosis in Parkinson's disease: signals for neuronal degradation. *Annals of Neurology*, **53 Suppl 3**: S61–S72.

Tillerson JL, Caudle WM, Reverón ME, et al. 2002. Detection of behavioral impairments correlated to neurochemical deficits in mice treated with moderate doses of 1-methyl-4-phenyl-1, 2, 3, 6-tetrahydropyridine. *Experimental Neurology*, **178**(1): 80−90.

Vidoni C, Secomandi E, Castiglioni A, et al. 2018. Resveratrol protects neuronal-like cells expressing mutant Huntingtin from dopamine toxicity by rescuing ATG4-mediated autophagosome formation. *Neurochemistry International*, **117**: 174−187.

Wan XX, Chowdhury IH, Jie ZL, et al. 2019. Origin of monocytes/macrophages contributing to chronic inflammation in chagas disease: SIRT1 inhibition of FAK-NFκB-dependent proliferation and proinflammatory activation of macrophages. *Cells*, **9**(1): 80.

Wang CY, Sun ZN, Wang MX, et al. 2018. SIRT1 mediates salidroside-elicited protective effects against MPP$^+$-induced apoptosis and oxidative stress in SH-SY5Y cells: involvement in suppressing MAPK pathways. *Cell Biology International*, **42**(1): 84−94.

Wang Y, Ouyang JH, Luo XJ, et al. 2021. Identification and characterization of novel bi-functional cathelicidins from the black-spotted frog (*Pelophylax nigromaculata*) with both anti-infective and antioxidant activities. *Developmental & Comparative Immunology*, **116**: 103928.

Wang YJ, Wang XY, Hao XY, et al. 2019. Ethanol extract of *Centipeda minima* exerts antioxidant and neuroprotective effects via activation of the Nrf2 signaling pathway. *Oxidative Medicine and Cellular Longevity*, **2019**: 9421037.

Watanabe Y, Kato H, Araki T. 2008. Protective action of neuronal nitric oxide synthase inhibitor in the MPTP mouse model of Parkinson's disease. *Metabolic Brain Disease*, **23**(1): 51−69.

Wei L, Yang JJ, He XQ, et al. 2013. Structure and function of a potent lipopolysaccharide-binding antimicrobial and anti-inflammatory peptide. *Journal of Medicinal Chemistry*, **56**(9): 3546−3556.

Wiriyaampaiwong P, Karnmongkol C, Punpad A, et al. 2022. Cathelicidin-HR from *Hoplobatrachus rugulosus*: an antioxidant peptide that performs a

protective effect against UV/H$_2$O$_2$ - induced DNA damage. *Journal of Applied Biology & Biotechnology*, **10**(4): 35−44.

Xu XQ, Lai R. 2015. The chemistry and biological activities of peptides from amphibian skin secretions. *Chemical Reviews*, **115**(4): 1760−1846.

Yang HL, Wang X, Liu XH, et al. 2009. Antioxidant peptidomics reveals novel skin antioxidant system. *Molecular & Cellular Proteomics*, **8**(3): 571−583.

Yang XW, Wang Y, Zhang Y, et al. 2016. Rich diversity and potency of skin antioxidant peptides revealed a novel molecular basis for high-altitude adaptation of amphibians. *Scientific Reports*, **6**: 19866.

Yao H, Xie Q, He QM, et al. 2022. Pretreatment with panaxatriol saponin attenuates mitochondrial apoptosis and oxidative stress to facilitate treatment of myocardial ischemia-reperfusion injury via the regulation of Keap1/Nrf2 activity. *Oxidative Medicine and Cellular Longevity*, **2022**: 9626703.

Yonezawa T, Hattori S, Inagaki J, et al. 2010. Type IV collagen induces expression of thrombospondin-1 that is mediated by integrin α1β1 in astrocytes. *Glia*, **58**(7): 755−767.

Zeng BS, Chai JW, Deng ZH, et al. 2018. Functional characterization of a novel lipopolysaccharide-binding antimicrobial and anti-inflammatory peptide in vitro and in vivo. *Journal of Medicinal Chemistry*, **61**(23):

10709−10723.

Zeng QY, Zeng BS, Chai JW, et al. 2020a. Antioxidant properties and neuroprotective effects of Esc-1GN through the regulation of MAPK and AKT signaling. *Life Sciences*, **254**: 117753.

Zeng XK, Xu K, Wang J, et al. 2020b. Pretreatment of ascorbic acid inhibits MPTP-induced astrocytic oxidative stress through suppressing NF-κB signaling. *Neural Plasticity*, **2020**: 8872296.

Zhang QS, Heng Y, Mou Z, et al. 2017. Reassessment of subacute MPTP-treated mice as animal model of Parkinson's disease. *Acta Pharmacologica Sinica*, **38**(10): 1317−1328.

Zhang Y, Wang QQ, Zhao Z, et al. 2021. Animal secretory endolysosome channel discovery. *Zoological Research*, **42**(2): 141−152.

Zhang YX, Wang M, Wei SS. 2010. Isolation and characterization of a trypsin inhibitor from the skin secretions of *Kaloula pulchra hainana*. *Toxicon*, **56**(4): 502–507.

Zhu ZH, Shi ZG, Xie CL, et al. 2019. A novel mechanism of Gamma-aminobutyric acid (GABA) protecting human umbilical vein endothelial cells (HUVECs) against H$_2$O$_2$-induced oxidative injury. *Comparative Biochemistry and Physiology Part C:Toxicology & Pharmacology*, **217**: 68−75.